An Experimental re-evaluation of Photon Mass Attenuation Coefficients

A Thesis Submitted to the

College of Graduate Studies and Research

in Partial Fulfillment of the Requirements

for the Degree of Master of Science

in the Department of Physics and Engineering Physics

University of Saskatchewan

Saskatoon

By

Cody Crewson

©Cody Crewson, February, 2013. All rights reserved.

PERMISSION TO USE

In presenting this thesis in partial fulfilment of the requirements for a postgraduate degree from the University of Saskatchewan, I agree that the Libraries of this University may make it freely available for inspection. I further agree that permission for copying of this thesis in any manner, in whole or in part, for scholarly purposes may be granted by the professor or professors who supervised my thesis work or, in their absence, by the Head of the Department or the Dean of the College in which my thesis work was done. It is understood that any copying or publication or use of this thesis or parts thereof for financial gain shall not be allowed without my written permission. It is also understood that due recognition shall be given to me and to the University of Saskatchewan in any scholarly use which may be made of any material in my thesis.

Requests for permission to copy or to make other use of material in this thesis in whole or part should be addressed to:

Head of the Department of Physics and Engineering Physics
163 Physics Building
116 Science Place
University of Saskatchewan
Saskatoon, Saskatchewan
Canada
S7N 5E2

ABSTRACT

Photon mass attenuation coefficients are indispensable input parameters for use in several disciplines. They are of value for medical diagnostics, radiation therapy, material science, etc. Currently, photon mass attenuation coefficients derived from model calculations are widely used. This project directly measured the photon mass attenuation coefficients of water and a number of water based solutions. These measurements were made using a High Purity Germanium (HPGe) detector allowing for increased resolution beyond traditional techniques. Four sources were used (^{133}Ba, ^{152}Eu, ^{137}Cs, ^{241}Am) producing multiple photons of interest over the range of 40 keV to 1.4 MeV, allowed for simultaneous collection of data and a refining of uncertainties beyond past techniques. Direct measurements using a new liquid technique supported the validity of Bragg's additive law, allowing for the mass attenuation coefficient of a constituent element to be calculated from a set of independent measurements. This technique allows materials not easily directly measured to be determined without an overburdening increase in uncertainty. The same direct measurements showed a deviation from the currently relied upon National Institute of Standards and Technology (NIST) database - XCOM. Investigations of the deviation and surrounding references showed XCOM being at most accurate to 5 % relative uncertainty.

ACKNOWLEDGEMENTS

I would like to extend a hard earned thank you to my supervisor, Chary Rangacharyulu, and another to the department.

I would also like to thank all of the people who have been referenced by this work. Any shortcomings of past experiments should be seen as the extreme change in technology, that if they had available at the time, would have been used.

This work is dedicated to all of the scientists that have come before, to all of those that have pushed the boundary of knowledge. May the future see this work bested, and bested again.

CONTENTS

List of Tables

LIST OF FIGURES

CHAPTER 1

INTRODUCTION

Science is the pursuit of describing that which we interact with. Over the last few hundred years the scope has changed, from attempting to quantify that which we can touch, see, and drop; to now quantifying the accuracy of our quantifications. With this drive for progress we have found out more. More what? More everything. From cosmology to entomology, from material science to particle physics, fields of study have grown more connected and more diverse. "Everything" is too large of a topic to approach, so let this discussion be limited to the act and results of measurement. Metrology is the field that concerns itself with precision and accuracy. Those interested in this field have proven beyond a doubt that understanding precision pushes boundaries, which leads to understanding the precision of the new boundaries. This cycle is progress; this cycle is discovery.

Discovery is not a new concept when applied to radiation. From the beginning, with the Curies and Becquerel, the progress of radiation has been tied to major advances in other fields. From imaging to communication, from medicine to astronomy, every eureka moment in radiation science has lead to real-world gains. One of the most memorable gains attributable to the physics department of the University of Saskatchewan, was the introduction of external radiation therapy, thanks in large part to Dr. Johns and Rt. Hon. Fedoruk. Their work in externalizing effective radiation sources for treatments increased the accuracy and assurances of dose measure, and delivery; saving lives around the world. As such this institution's ties to the application of physics as it relates to medicine have continued to foster further interdepartmental projects.

By always improving our ability to define our understanding, and concerning ourselves with the applications of the results of said studies, we are left with a self-imposed complication. There is a consistent issue for those that rely on experimental results: they are generally used without concern to how they were measured. This statement becomes more true the further separated the user and the scientist become. In the case of medical radiation sciences, this separation is nearly unwieldily large. Unavoidable as it may be, the end effect is that there are a number of values used which are extremely out of date. In general this is due to our ability to measure or predict a property value with increasing accuracy, with the advent of newer technology and time: yet our tendency to go back and remeasure past values wains. As such, using out-of-date information is in part due to our desire to explore new questions over revisiting past work, and in part due to the users of those values not reminding us that the old values are being used. This is not necessarily problematic, as most of the 'old' values used are of higher precision than needed for the given application. However as time and surrounding technology improves, this does not tend to remain true indefinitely.

Say there existed a magical algorithm which for our purposes relied on a single value. This value had an associated

5 % relative uncertainty. Twenty years ago, the algorithm was only solvable to around 20 %, for many reasons. As such, treating this value of import as exact had no real bearing on the result. Now, 20 years later, computers are orders of magnitude faster, so computers are finally fast enough to solve the algorithm exactly. Nevertheless the results are treated as exact, yet the algorithm relies on a non-exact value. As such there is a hidden uncertainty, long forgotten, limiting accuracy and precision.

One real-world analog of the above example is in medical imaging. Twenty years ago it would take days to evaluate 2-D skull images to a resolution of a centimetre. Today we can do whole body 3-D images with near millimetre resolution in less time. One value of import for reconstruction calculations is the attenuation factor. Section 1.1 will be devoted to defining this term, what is important now is that attenuation is an atomic property. There exists a database, XCOM: Photon Cross Section Database[1], which allows a user to search for any element or compound's attenuation coefficient. There is one large problem with XCOM: the authors make no attempt to quantify the precision or accuracy of the reported values. Four decades ago this was a necessary oversight, today, however, technology has improved enabling us with both the necessity and the ability to report and use interpolation uncertainties.

This report will concern itself with photons below 1.4 MeV, as the majority of terrestrial photon-electron interactions occur below that energy.

1.1 Attenuation

Attenuation describes the effectiveness of a material to impede a field or flux of photons, neutrons, or charged particles. This section will discuss photons, but it could be equally applicable to neutrons. Charged particle interactions add significant complexity and as such are usually discussed in terms of stopping power.

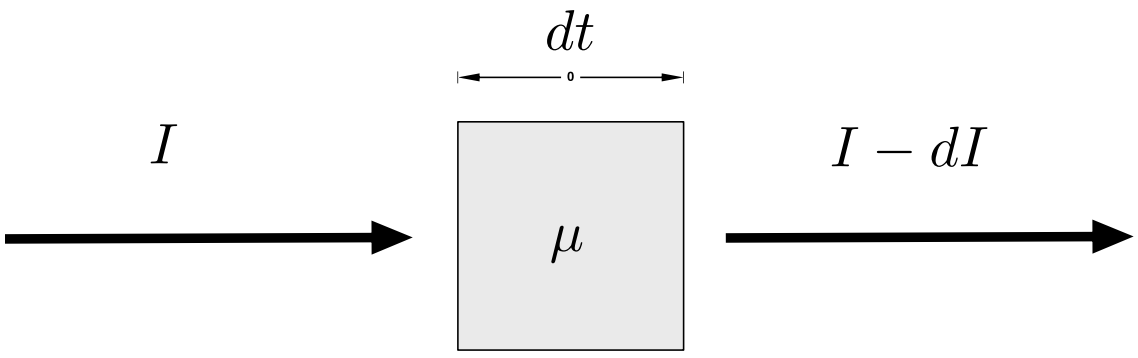

Figure 1.1: A thin material reducing the incident photon intensity, I, by dI

Attenuation, by definition, is the quantification of reduction of a signal due to an impediment. It could also be framed as the probility of loss due to interaction, since the interaction guarantees the photon is removed or redirected from it's initial direction. To quantify this we will start with a sheet so thin that there is no appreciable loss.

[1] XCOM is the formal name, not an acronym which can be found at `http://www.nist.gov/pml/data/xcom/index.cfm`

I is the initial intensity of photons incident on the thin sheet, dI is the number of photons lost and μ is the probability of attenuating a photon, so

$$dI = -\mu I dt \tag{1.1}$$

Now suppose we are to extend this to a thickness t, such that the loss is non-negligible. To do so we integrate over Equation 1.1.

$$\int_{I_0}^{I} \frac{dI}{I} = \int_{0}^{t} -\mu dt \tag{1.2}$$

which is

$$\ln\left(\frac{I}{I_0}\right) = -\mu t \tag{1.3}$$

or more nicely

$$I(t) = I_0 e^{-\mu t} \tag{1.4}$$

Since μ is the net effect of several processes, the relationship between μ and each of its following dependancies are very complex:

$$\mu \rightarrow \mu\left(Z, \rho, E_\gamma\right) \tag{1.5}$$

where Z is the atomic number, ρ is the density, and E_γ is the energy of the photon before the interaction. 'Before the interaction' is a necessary qualifier, as will be discussed in Chapter 2. Early experimentation relied on measuring μ for each combination of material and energy possible, while using pure metals at their room temperature density. This value is important for shielding and construction, where pure metals may be used, but is inconvenient in general. As such, Bragg proposed Bragg's Additive rule[2]:

$$\left(\frac{\mu}{\rho}\right) = \sum_i w_i \left(\frac{\mu}{\rho}\right)_i. \tag{1.6}$$

By dividing μ by the mass density, the new value $\left(\frac{\mu}{\rho}\right)$ is instead dependant on the number density of an element. Therefore, mixtures and compounds can be calculated by weighted addition of their constituent values. The weighting value w_i is determined by the relative weight of constituent i. The assertion of the additive nature of $\left(\frac{\mu}{\rho}\right)$ will be expanded on in Section 2.4.

1.1.1 Other Labels

Attenuation is not always discussed of in the form of Equation 1.4. Other forms include the half-value-thickness, $t_{1/2}$ or less commonly the $1/e$ value-thickness, $t_{1/e}$. Analogous to half-life, the half-value thickness is the thickness required

[2]This equation and its applications will be further explored in Section 2.4.

to reduce an incident field's power by a factor of $1/2$. Thus

$$\frac{I}{I_0} \equiv \frac{1}{2} = e^{-\mu t_{1/2}} \tag{1.7}$$

therefore

$$t_{1/2} = \frac{\ln(2)}{\mu} \tag{1.8}$$

Similarly, analagous to the mean life, the mean thickness is the thickness required to reduce incident intensity by a factor of $1/e$

$$t_{1/e} = \frac{1}{\mu} \tag{1.9}$$

$t_{1/2}$ is an important value for shielding, since the concern is not the accuracy of the amount of reduction from a source, but rather the capacity to reduce the peak intensity from a source to below a threshold, ensuring a minimum safety condition. However, while important, $t_{1/2}$ is not commonly used.

1.2 Applications of Data to Human Biology

Nuclear medicine relies on attenuation for both imaging and treatment. Most imaging is done with radiological tracers, and since the body is not homogeneous, the raw data needs to be corrected for the shape and density of the various components (muscle, bone) for an image to be reconstructed. This correction is done with attenuation coefficients.

The current common photon sources for diagnostic medicine are: [26, 21]

^{99m}**Tc** with a single significant (significant is defined for this work as > 1 % probability of the photon being emitted from any one decay) emission photon of 140 keV (89.06 ± 0.01 %)

^{131}**I** with four significant photons 284 keV (6.12 ± 0.06 %), 364 keV (81.5 ± 8 %), 636 keV (7.16 ± 0.10 %) and 723 keV (1.77 ± 0.03 %)

^{137}**Cs** with three significant photons 31.8 keV (1.99 ± 0.05 %), 32.1 (3.6 ± 0.1 %), and 661.7 keV (85.1 ± 0.1 %)

^{60}**Co** with two significant photons 1173 keV (99.85 ± 0.03 %), and 1332 keV (99.9826 ± 0.0006 %)

Other sources include rubidium-82, thallium-201, and fluorine-18. For scope, 80 % of all diagnostic imaging around the world currently relies on ^{99m}Tc. A significant portion of the remainder is done with PET, or positron emission tomography, a technique relying upon coincident detection of two 511 keV photons. The range of energies of interest to diagnostic medicine is thus between 30 and 1332 keV, with the focus on 140 and 511 keV.

To increase the precision of the attenuation coefficients for various human tissues Akar et al.[1] directly measured tissues and water, then compared their data with a past publication from the International Commission on Radiation Units and Measures (ICRU), Report 44[16]. As typical with other reports of the field, Akar et al. treats the values from

the ICRU report as exact, when in fact the report, while not stating an error, states that the values are not exact. The ICRU report, titled *Tissue Substitutes in Radiation Dosimetry and Measurement*, compares the calculated values for attenuation for the human body and various analogs. The direct measurements were made by slicing organic material to various thicknesses and placing it between a source and a detector, which resulted in attenuation coefficients with errors range between 5 to 20 %. This large error range can be improved upon.

CHAPTER 2

THEORETICAL UNDERPINNINGS

Attenuation is the measure of photon loss from the point of view of gross scale experimentation. It measures the probability of losing a photon through interaction. That statement has two points, probability and interaction. Mathematical physics has a measure of the probability of interaction, the cross section, σ, which describes the likelihood of interaction for any given situation. One great attribute of this value is that cross sections are additive, and if we can determine σ_i for each interaction, then we can determine the total cross section.

$$\sigma_{total} = \sum_i \sigma_i \tag{2.1}$$

As such, the ability to calculate the total cross section is dependant on the ability to calculate each individual cross section. Discussing every possible photon-electron interaction would be too large for this project's scope, as such this chapter will discuss the photo-electric effect and Compton scattering because they are the relevant interactions for the energy range 40 keV to 1.4 MeV. For the sake of completeness, pair-production will also be covered as the threshold for pair production interactions is 1.02 MeV; however the contribution of pair production below 2 MeV is always negligible. These discussions will include a visualization of the interaction, analytical solutions, and measurement techniques.

For the energy range of interest to this work, only the photoelectric and Compton cross sections are significant, so

$$\sigma_{total} = \sigma_{Compton} + \sigma_{photoelectric} \tag{2.2}$$

2.1 Photoelectric Effect

The photoelectric effect is the process whereby a photon is absorbed by an electron, freeing the electron and ionizing the atom or molecule from which the electron came. First formalized by Einstein in his 1905 paper "Über einen die Erzeugung und Verwandlung des Lichtes betreffenden heuristischen Gesichtspunkt," which translates to "On a Heuristic Point of View about the Creation and Conversion of Light"[7, 8]. Einstein simultaneously formalized the modern quantized photon and the interaction between the photon and the already partially-understood electron. While originally used to describe the mechanism of photovoltaics and the minimum wavelength required to liberate electrons, the physics extends to higher energy photons. We can find the energy of the electron and the minimum energy of the photon required to undergo this interaction.

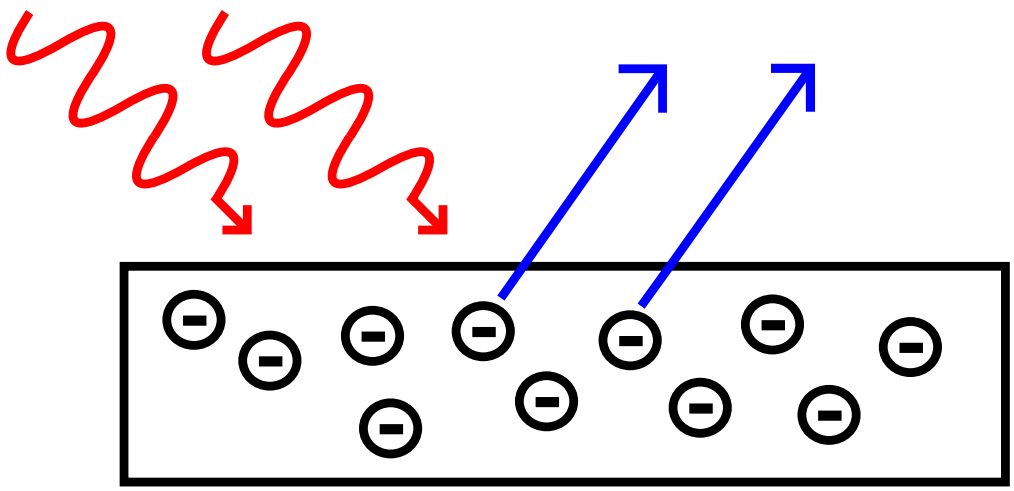

Figure 2.1: Photons ionizing atoms via the photo-electric effect

$$K_{max} = E_\gamma - \varphi \tag{2.3}$$

where φ is the minimum ionization energy and K_{max} is the kinetic energy of the electron. Einstein considered the situation where in a surface electron was ejected out of the material. For higher-energy interactions we need to look a little deeper.

A photon, in the range we are concerned with, will have a probability, $\sigma_{\text{photoelectric}}$, of forcing that electron to be ejected from the bulk material. As such the ejected electron will be subjected to charged particle-charged particle interactions with the bulk material. This has a number of implications that will be discussed later, but what should be noted now is that most often, the energy of the photon is entirely deposited into the bulk material. High energy gamma detectors rely upon this to for energy spectroscopy. In the case of solid state detectors, like the HPGe used in this experiment, the high resolution of the detector is achieved through high electrical signal to noise and through reliance on the photoelectric effect. The electron freed by the photon is trapped in a large potential difference that quickly converts one high energy electron to a large number of slightly excited electrons, the number of which is directly proportional to the energy of the incident photon.

No single equation has been found which can directly describe the cross section of a photo-electric absorption event based only on Z and photon energy, but Knoll [20] presents an approximation:

$$\sigma_{\text{photoelectric}} \propto \frac{Z^n}{E_\gamma^{3.5}} \tag{2.4}$$

where n is best approximated as 4 for lower energies and 5 for higher energies. This is a conceptual approximation of various empirical fit formulas used through various attempts to interpolate photoelectric cross section measurements. Interpolations and extrapolations from empirical data were a common way to expand the available data to predict cross sections for energies that had no available corresponding source or method. One equation for empirical fit is

$$\sigma_{\text{photoelectric}} \cong Z^5 \sum_{n=1}^{4} \frac{a_n + b_n Z}{1 + c_n Z} E^{-p_n} \left[\frac{\text{barns}}{\text{atom}}\right] \tag{2.5}$$

where a_n, b_n, c_n, and p_n are fit parameters. This fit formula can be used to solve for any relation of σ from Z^4 through Z^6. For the specific fit of $E > 0.2$ MeV and $13 < Z \leq 92$ the parameters were solved, as displayed in Table 2.1 [11]. These restrictions are because this empirical fit is for energies near or above the k-shell peaks with elements that have a significant electron shielding factor. For relatively low energies (below 0.5 MeV) the $n = 3$ term dominates and the $n = 4$ term is negligible, explaining Knoll's $E^{-3.5}$ dependance. As the energy increases, the $n = 1$ and 2 terms gain significance,

n	a_n	b_n	c_n	p_n
1	1.6268×10^{-9}	-2.683×10^{-12}	4.173×10^{-2}	1
2	1.5274×10^{-9}	-5.110×10^{-13}	1.027×10^{-2}	2
3	1.1330×10^{-9}	-2.117×10^{-12}	2.013×10^{-2}	3.5
4	-9.12×10^{-11}	0	0	4

Table 2.1: Fit parameters for the empirical fit formula for the photoelectric cross section, valid for $13 \leq Z \leq 92$ and $E \geq 0.2$ MeV

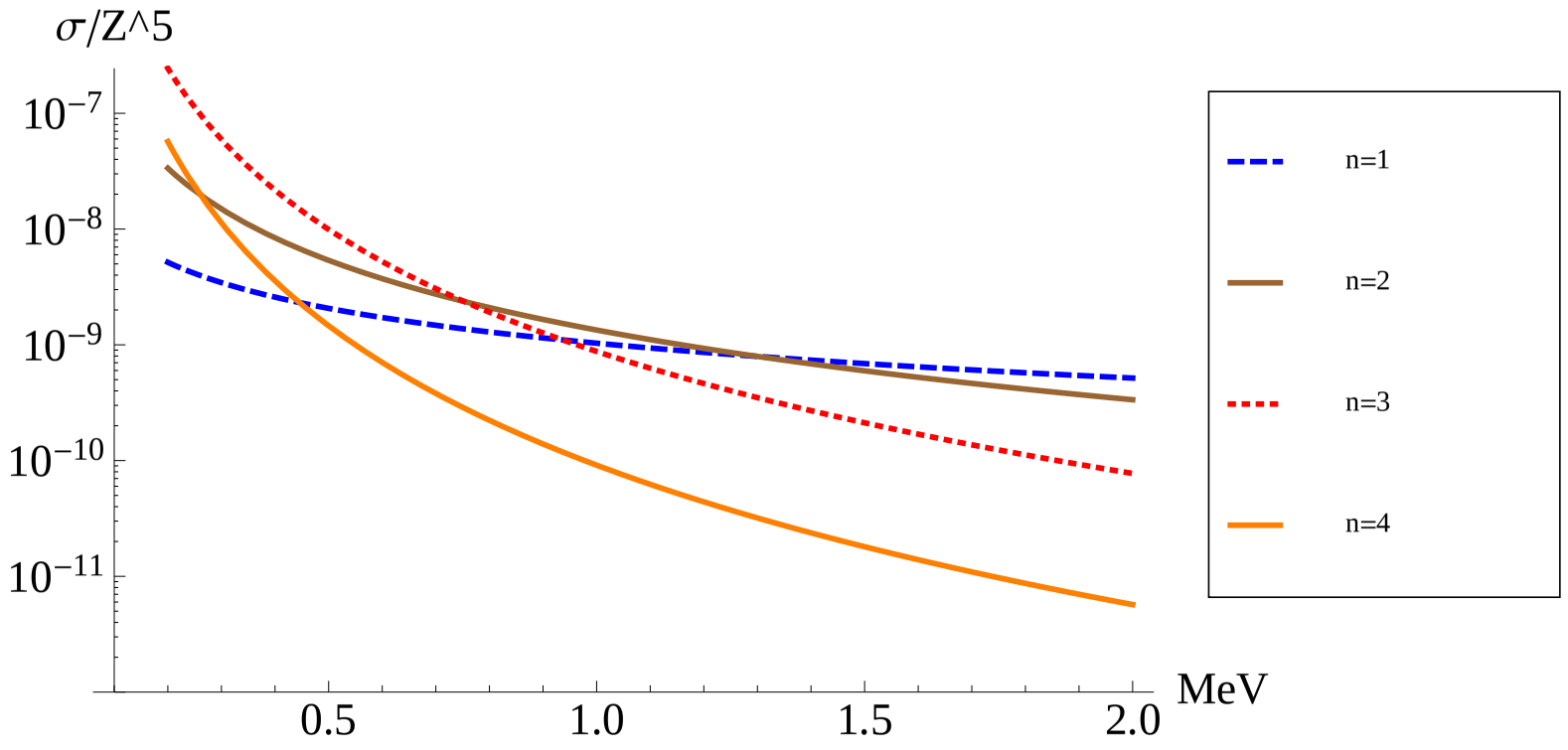

Figure 2.2: The magnitude of terms of the empirical fit formula for aluminum (Z=13) plotted over the energy range of 0.2 to 2 MeV. Note n=4 term is negative, only its magnitude has been plotted to allow for comparison.
For low energies the n=3 term dominates, resulting in $\sigma \propto \frac{Z^5}{E^{3.5}}$.
For high energies the n=1 term dominates resulting in $\sigma \propto \frac{Z^4}{E^1}$.
For the low Z case, the n=4 term is negligible over the entire energy range

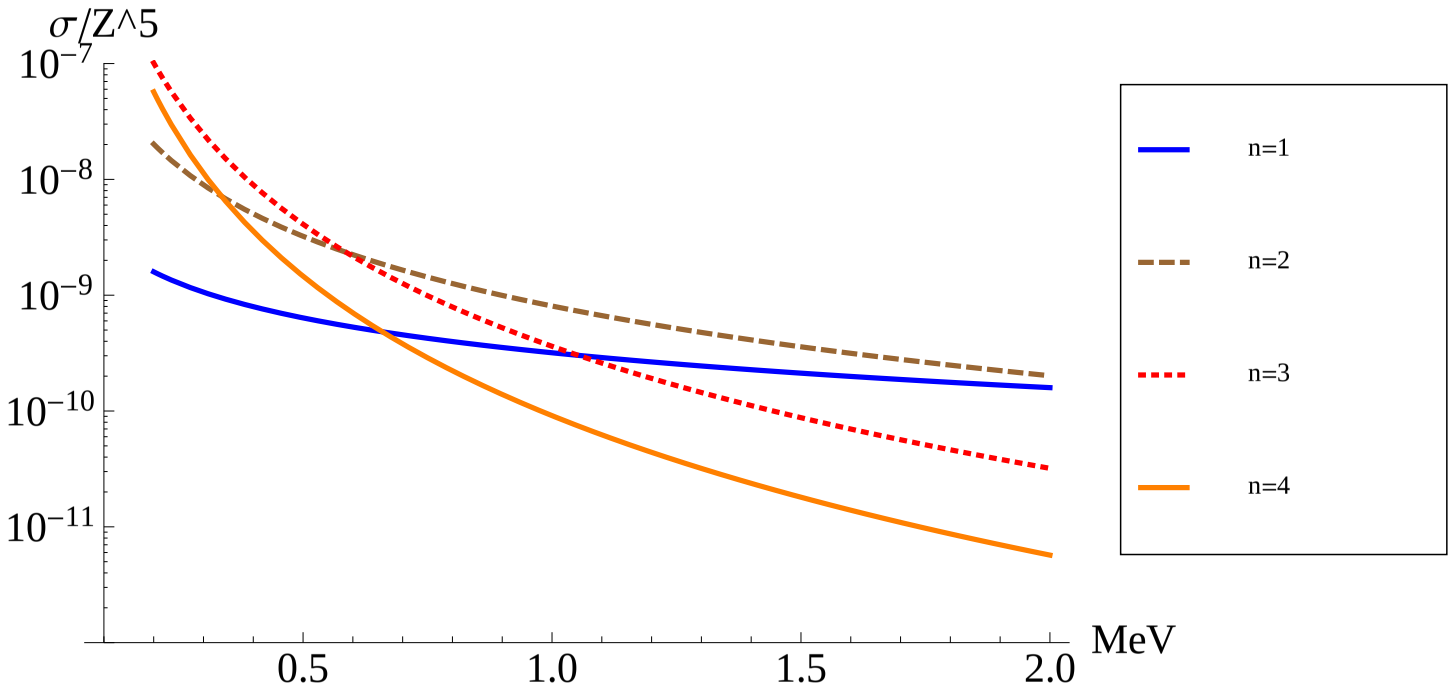

Figure 2.3: The magnitude of terms of the empirical fit formula for lead (Z=82) plotted over the energy range of 0.2 to 2 MeV. Note n=4 term is negative, only its magnitude has been plotted to allow for comparison.
For low energies the n=3 term dominates, resulting in $\sigma \propto \frac{Z^5}{E^{3.5}}$.
For high energies the n=2 term dominates resulting in $\sigma \propto \frac{Z^4}{E^2}$.
It should also be noted that for low energies the n=4 term is relevant, but for higher energies the term's contribution is negligible. As energy increases, the n=1 term's relevance increases from negligible to potentially significant.

Figure 2.2 and Figure 2.3 show the relative importance of each term in Equation 2.5 over the energy range of interest. The most significant feature is that for low energies, where the photo-electric effect is dominant, $\sigma \propto \frac{Z^5}{E^{3.5}}$.

Let us look at a single photon and bound electron of a large Z atom. The probability for that photon to excite that electron has a number of dependencies. If the energy of the photon is below the minimum excitation energy of the electron then the photon will not be absorbed. The probability is highest when the photon is just above the threshold needed to ionize that electron and quickly drops off as energy increases. These spikes in probability result in what is referred to as resonance peaks within the data. The rightmost peak on Figure 2.4b illustrates this effect. The minimum ionization energy of electrons will change depending on molecular interactions, and as such these resonance peaks can shift depending on the element, and the strength of the molecular bond.

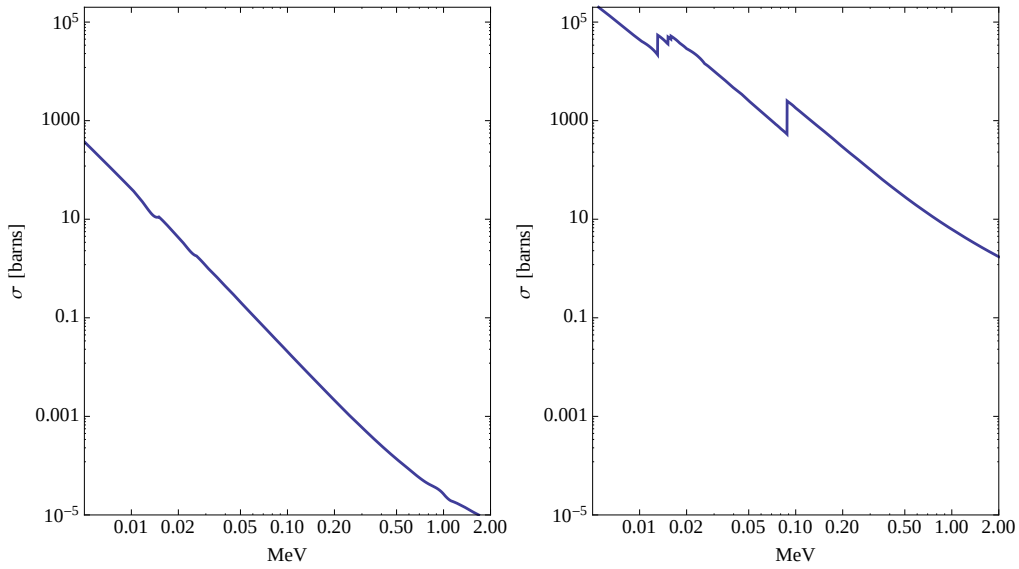

(a) Carbon **(b)** Lead

Figure 2.4: Carbon (Z=6) and Lead(Z=82) photo-electric coefficients plotted for the energy range 5 keV to 2 MeV [22]. It is seen that cross section for Z=82 are at least a factor of 100 greater than for Z=6 elements for any given energy. Also seen in Z=82 are distinct photo-absorption peaks at energies below 100 keV.

Figure 2.4 shows a few important features. In addition to the inner shell resonance peaks seen in Figure 2.4b, the general trend of cross section reducing as photon energy is clearly demonstrated. By comparing the scales of the carbon and lead plots, the change in carbon photo-electric cross section is far steeper than that of lead.

Since there is no way to generate one single expression, it adds complexity to any predictive model for determining the cross section. This photon electron interaction is the dominant interaction from the minimum ionization energy of the material to between about 100 keV and 2 MeV, depending upon the target material. This is due in part to the relative contributions of other effects, but more significantly, is mostly due to the absolute drop in probability of a photo-electric capture occurring as the photon's energy greatly exceeds the binding energy of the innermost electrons. This drop off can be seen from Equation 2.4's photon energy term being in the denominator, so as the energy increases, the probability must decrease.

2.2 Compton Scattering

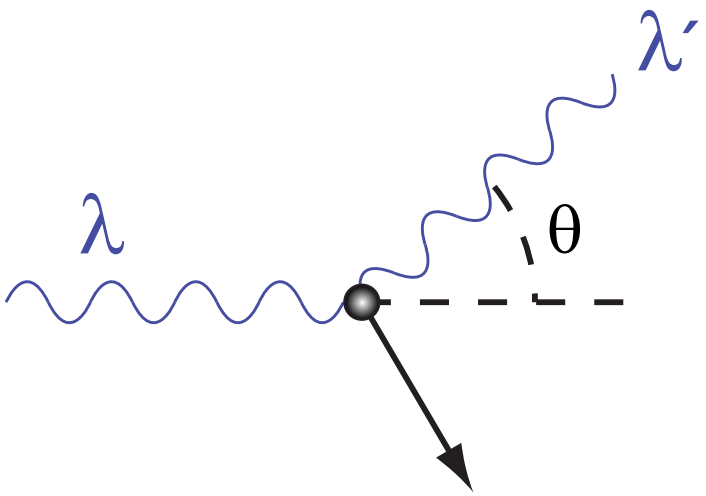

Figure 2.5: A single photon loosing energy and changing direction due to Compton scattering

Compton scattering is an elastic collision between a photon and an electron. First discovered by Arthur Holly Compton in 1922, and described in his 1923 paper "A Quantum Theory of the Scattering of X-rays by Light Elements"[3]. He would be awarded the Nobel Prize in Physics in 1927 for the discovery. A photon of sufficient energy will scatter off of an electron. Since the total momentum of the interaction is conserved and the electron is ejected, the photon transfers momentum to the electron. Thus the photon must have less energy, or as originally described, a longer wavelength. The idea of measuring a photon as a wave but treating the interaction as a particle-particle interaction cemented the wave particle duality theory that we rely upon today. The interaction between the photon's incident wavelength λ and resultant wavelength λ' can be described by

$$\lambda' - \lambda = \frac{h}{m_e c}(1 - \cos\theta) \tag{2.6}$$

where h is plank's constant, m_e is the mass of the electron, c is the speed of light, and θ is the scattering angle. In terms of energy this becomes

$$E' = \frac{E}{1 + \frac{E}{m_e c^2(1-\cos\theta)}} \tag{2.7}$$

since

$$E = \frac{hc}{\lambda}. \tag{2.8}$$

Since the photon is scattered and has a lower energy, the interacting photon is considered to be attenuated. This process has a relatively significant probability of occurring, when compared to other processes, from as low as 100 keV to as high as a few GeV. The differential cross section solution, used to describe the likelihood of a photon being scattered

at a specific θ can be seen in the Klein-Nishina Formula, Equation 2.9. Klein and Nishina derived the formula from kinematics and quantum electrodynamics, for unbound electrons. This equation has been modified to produce the KN cross section in relation to the atomic number, Z. [**?**]

$$\frac{d\sigma_{K-N}}{d\Omega} = Zr_0^2 \left(\frac{1}{1+\alpha(1-\cos\theta)}\right)^2 \left(\frac{1+\cos^2\theta}{2}\right) \left(1+\frac{\alpha^2(1-\cos\theta)^2}{(1+\cos^2\theta)(1+\alpha(1-\cos\theta))}\right) \tag{2.9}$$

Notice the dependance on Z, the number of protons, r_0, the classical electron radius, θ, the scattered angle of the photon with respect to it's incident trajectory, and α described by

$$\alpha = \frac{E_\gamma}{m_0 c^2} \tag{2.10}$$

where E_γ is the incident photon energy. Figure 2.6 is the polar form plot of the relative distributions from Equation 2.9 for various energies.

In Figure 2.6, the distance from the origin along any angle corresponds to the relative likelihood of a photon to be scattered in that direction when compared to other directions for a photon of the same energy. This plot has been normalized so that the forward scatter peak at zero degrees is the same intensity for all energies plotted. Of important note are a few features: as the photon energy increases the relative amount of radiation scattered back past 90° decreases; at low energies the scattering distribution is peanut shaped; and as the energy increases it progressively approaches an ellipse. This trend follows from the limits of $E_\gamma \to 0, \infty$,

$$\lim_{E_\gamma \to 0} \frac{d\sigma_{K-N}}{d\Omega} = Zr_0^2 \left(\frac{1+\cos^2\theta}{2}\right) \tag{2.11}$$

which has the peanut shape illustrated in the 0 eV line of Figure 2.6.

For $E_\gamma \to \infty$

$$\lim_{E_\gamma \to \infty} \frac{d\sigma_{K-N}}{d\Omega} = \frac{Zr_0^2}{2\frac{E_\gamma}{m_0 c^2}(1-\cos\theta)} \tag{2.12}$$

which has a elliptic shape. Appendix A.1 shows the full derivation of the above two limits. To determine the Klein-Nishina Compton cross section from $d\sigma_{K-N}$,

$$\sigma_{\mathrm{K-N}} = \left(\int \frac{d\sigma_{K-N}}{d\Omega} d\Omega\right) \tag{2.13}$$

To illustrate the trend of increase of forward scattering, Table 2.2 shows

$$\sigma_{\text{partial}} = \frac{\int_{\Omega=-\frac{1}{12}}^{\frac{1}{12}} \frac{d\sigma_{K-N}}{d\Omega} d\Omega}{\int_\Omega \frac{d\sigma_{K-N}}{d\Omega} d\Omega} \text{ and } \sigma_{\text{partial}} = \frac{\int_{\Omega=-\frac{1}{6}}^{\frac{1}{6}} \frac{d\sigma_{K-N}}{d\Omega} d\Omega}{\int_\Omega \frac{d\sigma_{K-N}}{d\Omega} d\Omega}$$

corresponding to the partial probability if scattered, of scattering within 30°, and 60° cones about the 0° axis.

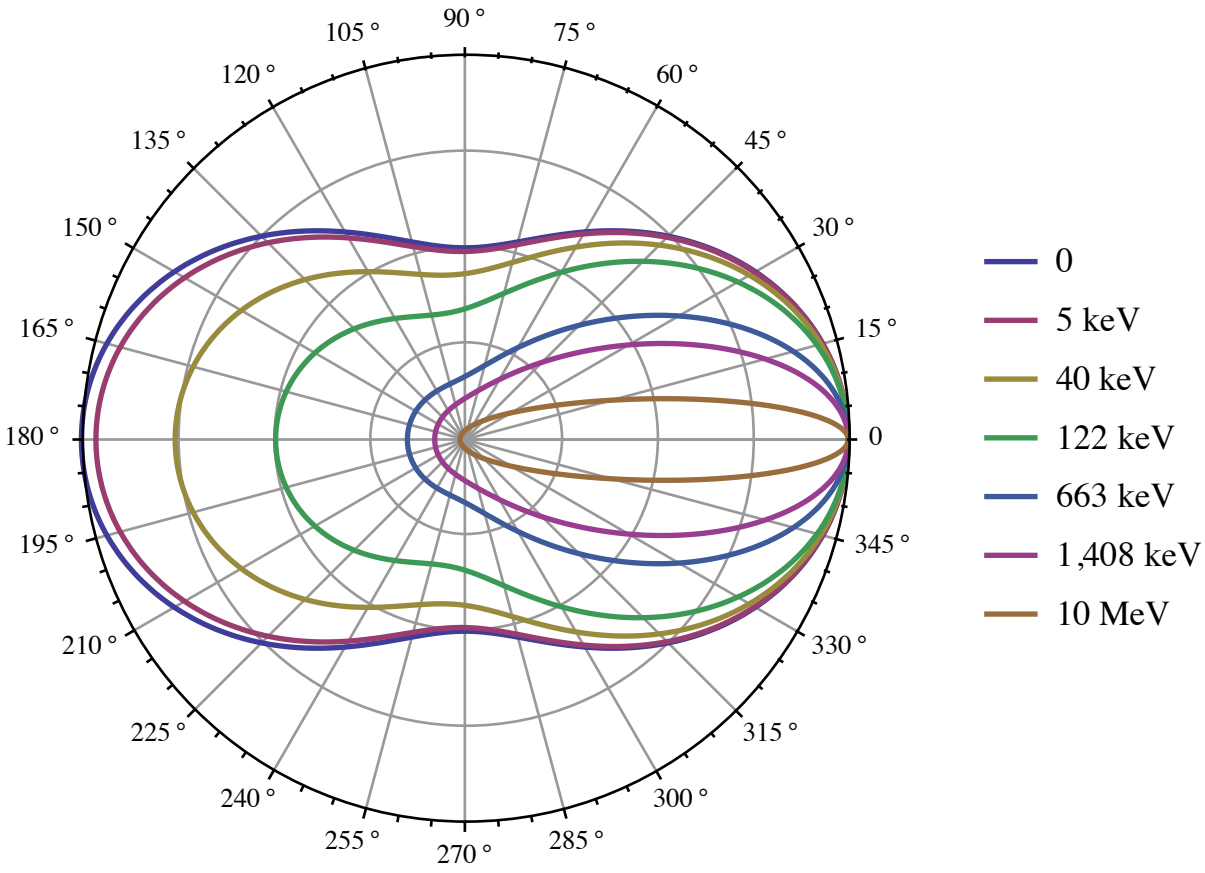

Figure 2.6: Klein-Nishina distribution plotted on a 360-degree intensity plot for various photon energies from 0 eV to 10 MeV. For the limit of $E_\gamma = 0$ eV, Klein-Nishina predicts equal probabilities of scattering less than or greater than 90-degrees. As the energy increases the distribution shifts shape and weight such that for high energies most scattering is within the forward 30-degree cone. Of note to this graph is that Compton scattering is dominant from between about $E_\gamma = 50$ keV and $E_\gamma = 1.5$ MeV (Z dependant), depicted within the yellow and pink lines.

E [MeV]	-15° to 15°	-30° to 30°
0	0.110	0.213
0.005	0.112	0.217
0.040	0.126	0.242
0.122	0.152	0.290
0.663	0.246	0.443
1.408	0.314	0.532
10	0.571	0.757

Table 2.2: Comparison of the fraction of photons scattered within a 30° cone and a 60° cone about the 0° axis. The progression shows that as the energy increases the majority of Compton scattered photons are scattered within the forward 60° cone, with a significant portion of that scattering contained within the 30° cone.

2.2.1 Verification of Klein-Nishina

To verify the validity of the Klein-Nishina formula for total cross section, Figure 2.7 was generated, comparing the Klein-Nishina cross section with XCOM's Compton cross section. The plot of the Klein-Nishina cross section was calculated using mathematica (see Appendix B.1).

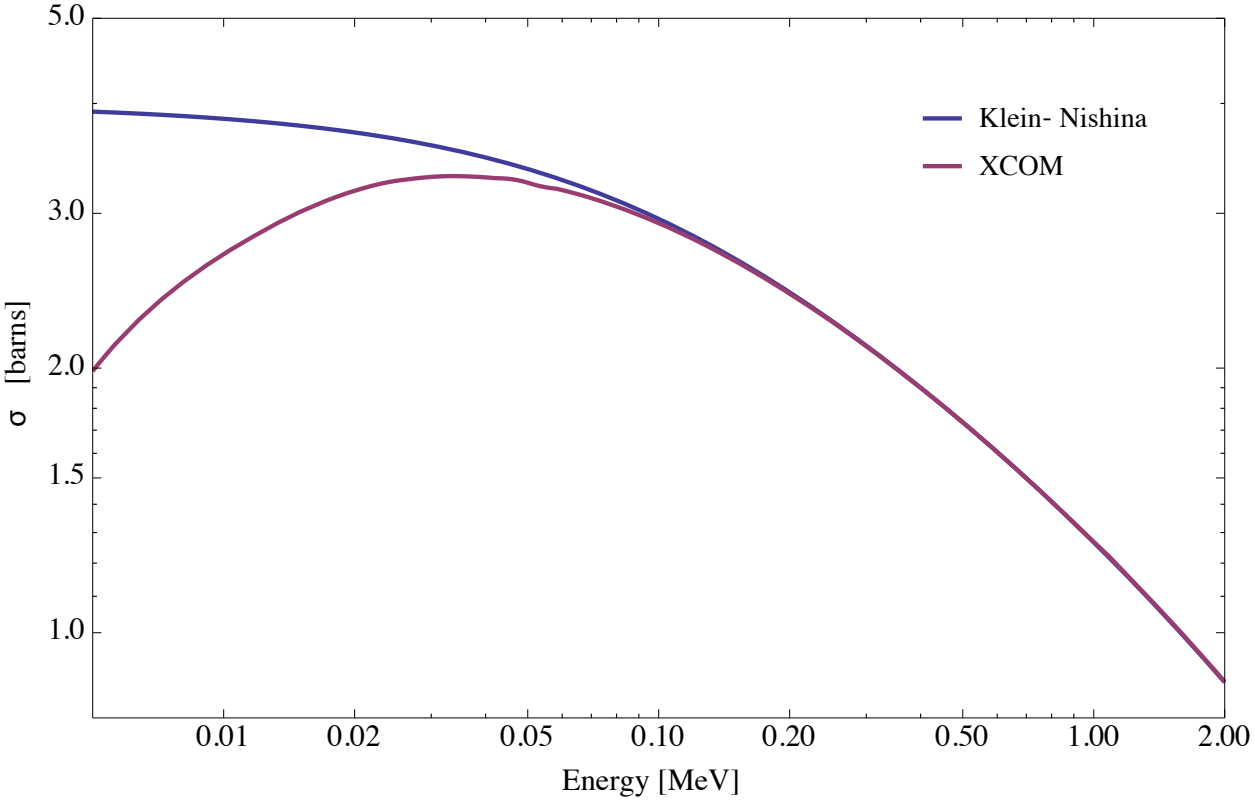

Figure 2.7: Comparison of the Klein-Nishina cross section and XCOM Compton cross section for carbon ($Z = 6$), between 0.005 and 2 MeV. The limit of $E_\gamma = 0$ for the Klein-Nishina cross section agrees with the Thompson scattering limit value of 0.66 barns/electron.

Figure 2.7 shows that the assumption of treating the electrons as isolated charged particles cannot sufficiently solve the dynamics of Compton scattering. A number of correction factors need to be incorporated to correct the Klein-Nishina approximation such that it agrees with the experimental trend which XCOM's Compton cross section of carbon illustrates. These corrections, including the form factor correction, $S(q,Z)$, are based on the electrical structure of each element and momentum transfers for bound electrons. As such they are dependant on measurements and no longer based on a free electron.

Figure 2.8 shows the relatively smooth and featureless cross section plots for both carbon and lead calculated according to Hubbell [15]. Features to note are the peak location, and maximum value. Carbon peaks at around 40 keV and 0.2 cm^2/g; lead at about 100 keV and 0.1 cm^2/g. Since the cross section increases with Z, and decrease as E_γ increases, E_γ is the more important term of the two.

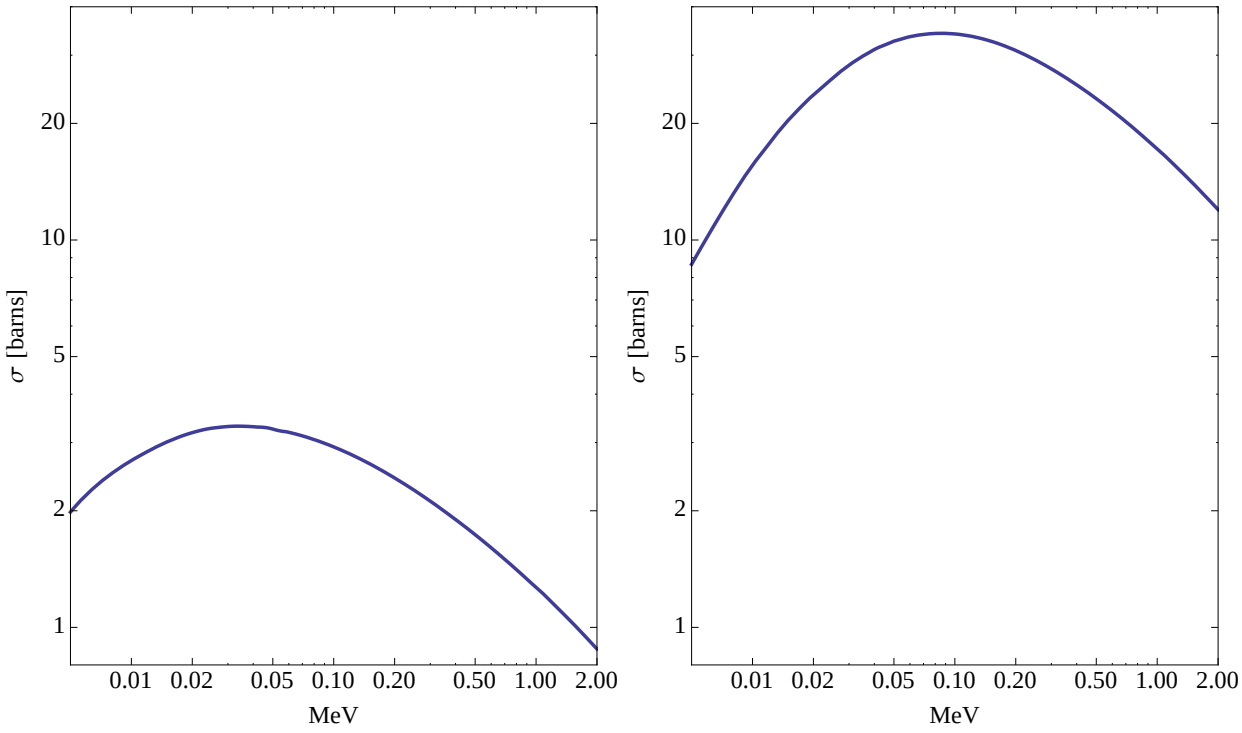

(a) Carbon cross section

(b) Lead cross section

Figure 2.8: Carbon ($Z = 6$) and lead ($Z = 82$) Compton coefficients plotted for the energy range 5 keV to 2 MeV [22].

2.3 Pair Production

Pair production is the process by which a photon is perturbed by an electric field, transforming into a particle and its anti-particle. The threshold photon energy for this to occur is twice the rest energy of the particle. Since the electron's rest energy is 511 keV, the minimum photon energy required to produce an electron-positron pair is 1.022 MeV. The likelihood of pair-production occurring is dependant on the charged particle density and on the energy of the photon, since the decay is due to the photon being perturbed by a point charge. The charge could be either an electron (negative) or an atom's nucleus (positive). The nucleus has a greater effect at lower photon energies, due to the nucleus' higher charge concentration producing a larger volume for which the electromagnetic field is strong enough to perturb the photon. As expected, momentum and energy are conserved in this decay.

This conservation of momentum adds a further complication. When the decay is induced by a nucleus the momentum transfer to said nucleus due to recoil interactions is negligible. Since the electron's mass is much smaller than even a single proton, the momentum transfer for electron induced pair-production becomes important. Borsellino and Votruba used this momentum transfer to determine a new minimum photon energy threshold of 4 electron masses ($E_\gamma = 4 \times 0.511$ MeV $= 2.044$ MeV for electron induced pair production, as summarized by Joseph [17].

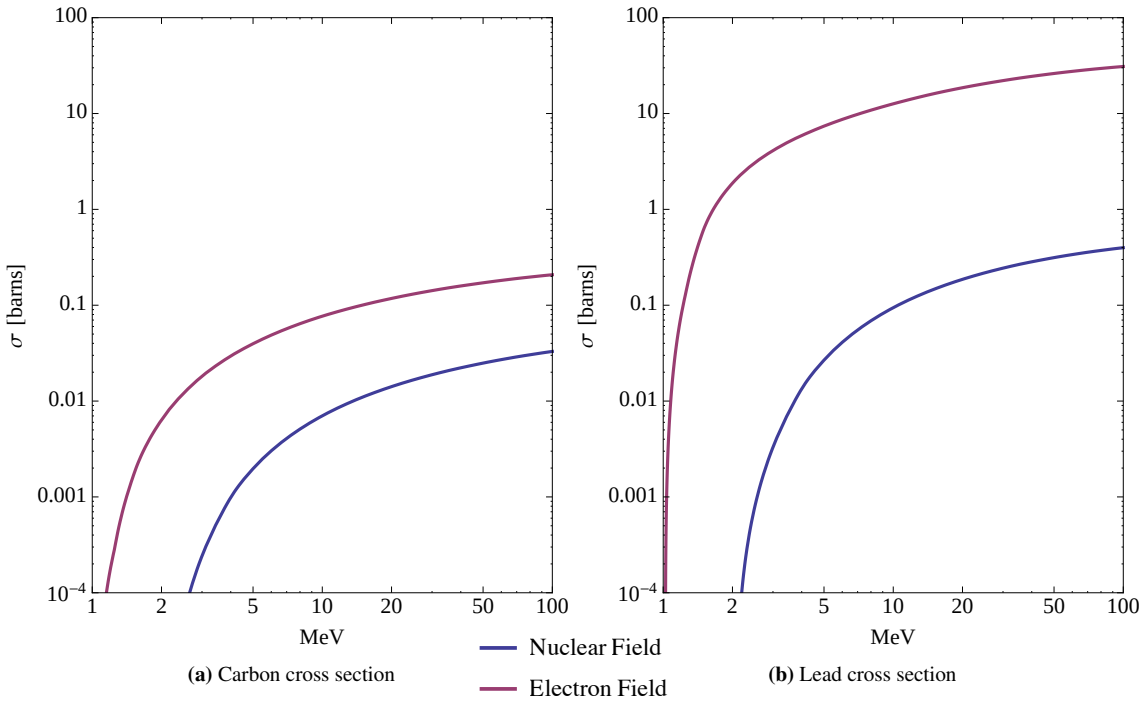

(a) Carbon cross section

(b) Lead cross section

Figure 2.9: Carbon (Z=6) and Lead(Z=82) pair-production cross sections plotted for the energy range 1 to 100 MeV [22].

2.4 Bragg's Additive Law

The idea of linear attenuation coefficients proved to be extremely useful in the early days of radiation experimentation. Mass attenuation coefficients further extended the usefulness of this information by increasing comparability and providing a method to adjust for different situations with the same material. For example, instead of directly measuring the attenuation of steam, one could simply predict it by measuring the attenuation of water and correcting for variance in density.

It was shown that the mass attenuation is related to another property of each element, the photon cross section. Since the cross section describes the probability of a photon interacting with an atom's electron cloud based on the properties of that atom, the relation is expected.

$$\left(\frac{\mu}{\rho}\right) = \frac{N_a}{A}\sigma_{\text{total}} \tag{2.14}$$

where N_a is Avogadro's number, and A is the atomic weight. Since the total cross section is known to be

$$\sigma_{\text{total}} = \sum_i w_i \sigma_i, \tag{2.15}$$

Where w is the weighting factor for each constituent cross section. For types of cross sections that are independant, say Compton and photo-electric, $w_{\text{Compton}} = w_{\text{pairproduction}} = 1$. For displacement additions, say mixing, the weighting factor is the relative mass contribution. Bragg asserted that the mass attenuation coefficients should also be additive, thus

$$\left(\frac{\mu}{\rho}\right) = \sum_i w_i \left(\frac{\mu}{\rho}\right)_i \tag{2.16}$$

For example, if we had a mechanical mixture of 40 % copper by mass and 60 % aluminum by mass, then the equation would be

$$\left(\frac{\mu}{\rho}\right)_{\text{CuAl}} = 0.4\left(\frac{\mu}{\rho}\right)_{\text{Cu}} + 0.6\left(\frac{\mu}{\rho}\right)_{\text{Al}} \tag{2.17}$$

This additive law is useful for prediction and analysis; however, it is built upon the assumption that the atom's electron structure does not change. This is due to mass attenuation being a fixed measured quantity with no way to correct for shifts in resonance photo-absorption peaks due to molecular bonding shifting the electron orbital energies. B.R. Kerur has two studies [19, 18] testing the validity of Bragg's additive law at various energy ranges. Kerur showed that Bragg's law does not hold for all energies and elements. It does break down when the resonance absorption peaks shift due to the changes in electron orbital energies from bonding. Kerur's work does also show that further from the resonance peaks, and when Compton scattering is dominant, Bragg's assertion agrees with experiment, and thus is useful in most situations above 100 keV without concern of correction.

2.5 XCOM

XCOM is a heavily relied-upon database, from which the values supplied to the user are calculated. Photoelectric cross sections are calculated using Scofield's solutions [24], themselves a subset of Hartree-Fock solutions for electron ionization through photon capture. The values are cross referenced with empirical fit formulas to normalize unsolvable parameters and check for agreement. Compton cross section calculations are based on various works which solve Compton scattering using Hartree-Fock, Hartree-Slater, and Klein-Nishina methods [25]. Pair production is found through various works summarized in Hubbell's 1980 paper [14]. These, combined with the coherent (Rayleigh) scattering and nuclear photo-absorption cross sections are summed to produce the values recalled. Attenuation coefficients are accessed by inputing the desired element or compound and energies.

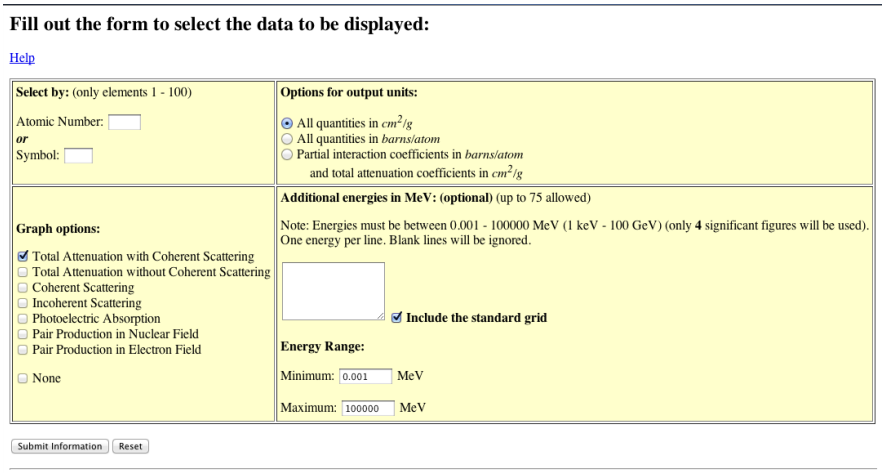

(a) Element

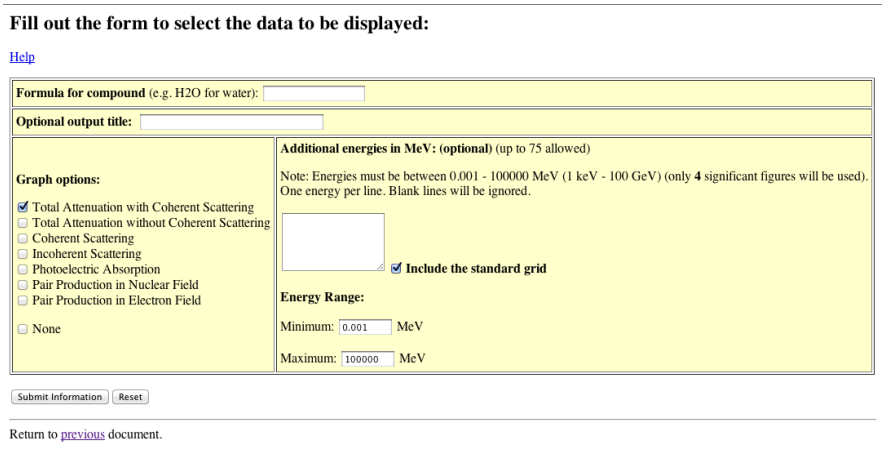

(b) Compound

Figure 2.10: XCOM input sheet for elements and compounds. To use, an element or stochiometric formula must first be entered, then a graph, range of interest and specific energies can be called. In addition Figure 2.10a will output in either units of cm^2/g, corresponding to mass attenuation coefficients; or in barns/atom, corresponding to cross section [22].

The screen shown in Figure 2.10a allows one to select the desired element and photon(s) of interest. The form in Figure 2.10b provides the same for compounds, like water. XCOM returns a plot, Figure 2.11, of the attenuation compared with energy, and a table, Figure 2.12, listing both a default list of values and any requested values from Figure 2.10. These values were calculated from a combination of equations and normalization parameters.

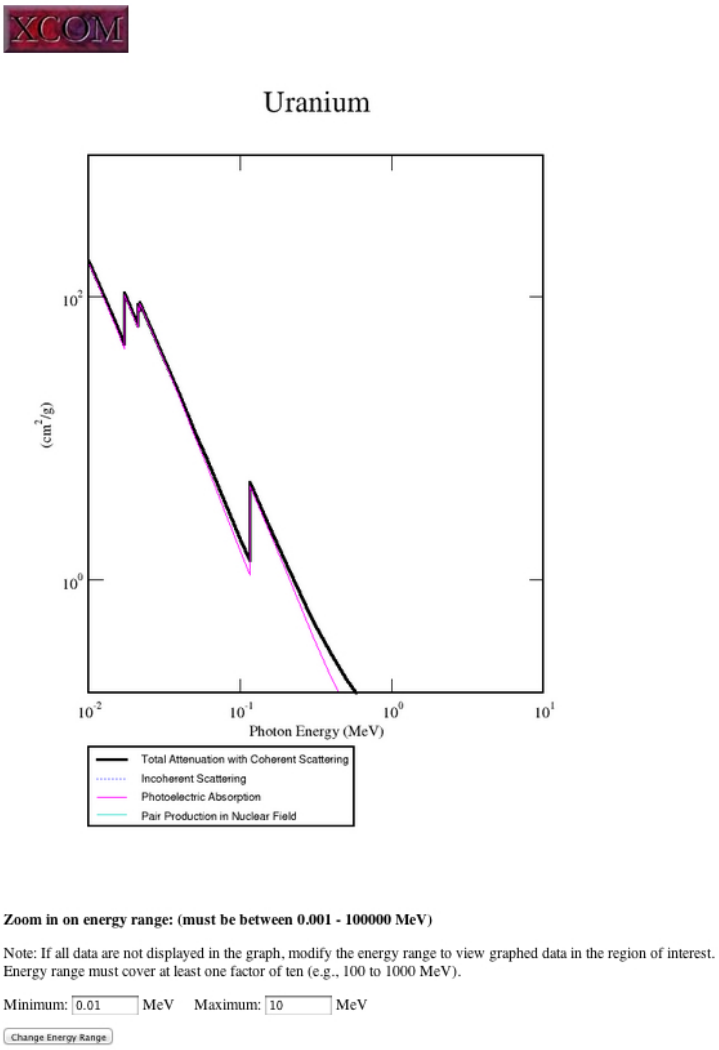

Figure 2.11: Standard XCOM graph output for the mass attenuation of uranium [22]

The various solutions for the mass attenuation coefficients over various energy ranges were originally fixed to observations by normalization with experimental data from before 1970 over the energy range 1 keV to 10 MeV [12]. This means that XCOM is a model based database, and thus susceptible to the models' assumptions. The primary assumption would be how the photoelectric effect's contribution changes with photon energies close to the binding energies of the electrons. The other important assumption is which regions each photon-electron interaction is dominant with respect to the energy of the photons and the number of electrons. While the trends may be predictable, fine structure may appear in experimentation that is not predicted by theory which would be important for applications. These regions of uncertainty overlap the regions currently used by medical applications [23, Section 27.4].

Sodium iodide detectors are at best far lower resolution than the current standard HPGe detectors similar to the one used in this project. The current multichannel analyzers allow for concurrent data collection of what would have been done in series in the 1970's, thus many sources of systematic and random error are reduced or removed from the data analysis. The lower resolution and longer data collection periods also required advanced curve separation techniques for photon energies that would produce overlapping signals. The need for such techniques can be avoided by using high resolution detectors and carefully selecting multiple sources to select a set of photons that provide the range of interest without any peaks of interest overlapping.

Figure 2.13 shows the calculated relative contributions of the Photoelectric effect and Compton scattering towards

Atomic Number : 92

To download data in spreadsheet (array) form, choose a delimiter and use the checkboxes in the table heading. After downloading, save the output by using your browser's `Save As` feature.

Delimiter:

- (•) space
- ( ) | (vertical bar)
- ( ) tab
- ( ) newline

Download data | Reset

Edge	(required) Photon Energy	Scattering		Photoelectric Absorption	Pair Production		Total Attenuation	
		Coherent	Incoherent		In Nuclear Field	In Electron Field	With Coherent Scattering	Without Coherent Scattering
	MeV	cm^2/g	cm^2/g	cm^2/g	cm^2/g	cm^2/g	cm^2/g	cm^2/g
	1.000E-02	5.498E+00	4.397E-02	1.736E+02	0.000E+00	0.000E+00	1.791E+02	1.736E+02
	1.500E-02	3.734E+00	5.705E-02	6.148E+01	0.000E+00	0.000E+00	6.527E+01	6.154E+01
	1.717E-02	3.218E+00	6.143E-02	4.334E+01	0.000E+00	0.000E+00	4.662E+01	4.340E+01
92 L_3	1.717E-02	3.218E+00	6.143E-02	1.037E+02	0.000E+00	0.000E+00	1.070E+02	1.037E+02
	2.000E-02	2.689E+00	6.626E-02	6.831E+01	0.000E+00	0.000E+00	7.107E+01	6.838E+01
	2.095E-02	2.540E+00	6.770E-02	6.039E+01	0.000E+00	0.000E+00	6.300E+01	6.046E+01
92 L_2	2.095E-02	2.540E+00	6.770E-02	8.577E+01	0.000E+00	0.000E+00	8.837E+01	8.583E+01

Figure 2.12: Standard XCOM table output for the mass attenuation coefficient of uranium, if extra energies were requested, the corresponding lines would be blue [22]

the total mass attenuation for the energy region of interest to this project (5 keV to 2 MeV). For the low Z element, carbon, the crossover region is narrow and between 10 and 50 keV. For the high Z element, lead, the crossover region is less defined, and centres about a higher energy of about 800 keV. These two graphs illustrate that as the number of electrons increases, the probability of photoelectric interactions increase. Additionally photons that are well beyond the highest electron escape transitions for an element are unlikely to be absorbed. These two interactions mean that the solving for the total mass attenuation cross section near the cross-over regions must introduce complexity. This complexity can introduce discrepancies between theory and experiment.

The XCOM database not only contains element mass attenuation values, but also the mass attenuation values for compounds and mixtures. Mixtures are calculated by Bragg's Additive Law, Equation 2.16.

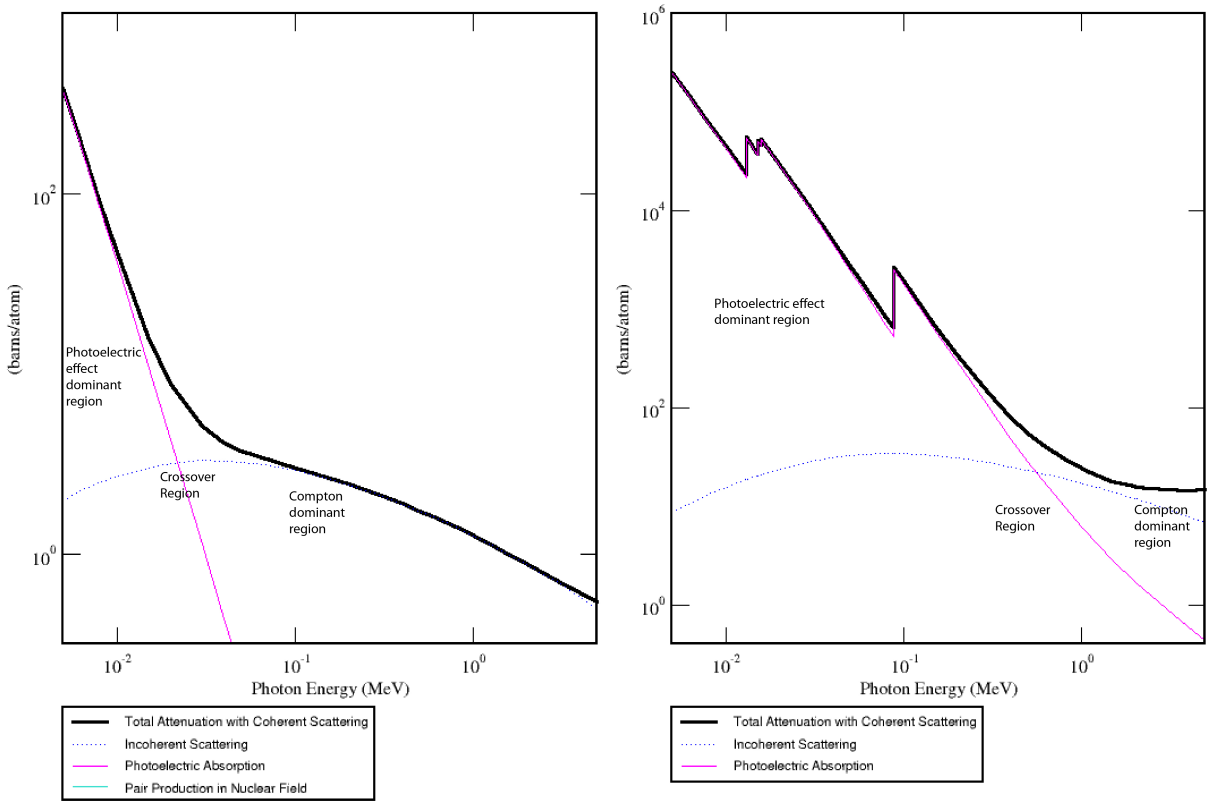

(a) carbon cross section

(b) lead cross section

Figure 2.13: Carbon (Z=6) and lead (Z=82) total attenuation coefficients plotted with relative Photoelectric effect and Compton scattering contributions for the energy range 5 keV to 5 MeV [22].

CHAPTER 3

PAST EXPERIMENTS

To better understand the current methods and practices, a look back at the methods used to collect the data relied upon for XCOM, and for other similar resources of the era, is required. Gopal and Sanjeevaiah describe in detail the methods used to collect experimental data for photon mass attenuation coefficients [9]. Modern methods have allowed for great advancement in source selection, detection, and analysis.

To avoid complications in analysis, when possible, single photon sources with long half-lives were preferred. The iconic example is ^{137}Cs, with a dominant photon at 662 keV and relatively low intensity cluster of X-rays below 33 keV. Isolating and collimating the source such that a uniform field of 662 keV was incident upon the target was well within the capabilities of the time, and as such ^{137}Cs was considered to be a single photon source. Extending the ^{137}Cs methods to the entire high energy x-ray and gamma energy photon spectrum was not possible since there are not enough long half-life radioactive isotopes that could be considered single photon sources to cover the range of interest with the desired fine resolution. Shorter half-live sources were then used to attempt to fill the gaps between the ideal source, however these required half-life adjustments to the recorded data, introducing extra uncertainties. When no single photon sources could be used, multi gamma sources were, however these required additional analysis that further increased the uncertainty.

To quantify the additional uncertainties introduced from the use of multiple photon sources, a strong understanding of the detection system is needed. In contrast to modern detectors, which produce fine energy resolution measurements, and multichannel analyzers capable of recording and profiling the detector's entire output, previous systems relied on lower resolution detectors and single channel analyzers.

In 1973 the standard available equipment included Sodium-Iodide scintillators, photomultiplier tubes, single channel analyzers and scalar counters. Figure 3.1 shows two typical setups used. There are a few features of note:

- A NaI crystal attached to an accompanying photomultiplier tube was used to detect the photons and generate a corresponding electrical signal.
- The amplification and counting circuit used to measure the intensity included a pre-amplifier, amplifier, single channel analyzer, and scalar.
- Collimators were needed to ensure that all photons detected would have had to have travelled in a straight line from the source through the target to the detector, with no deflection.

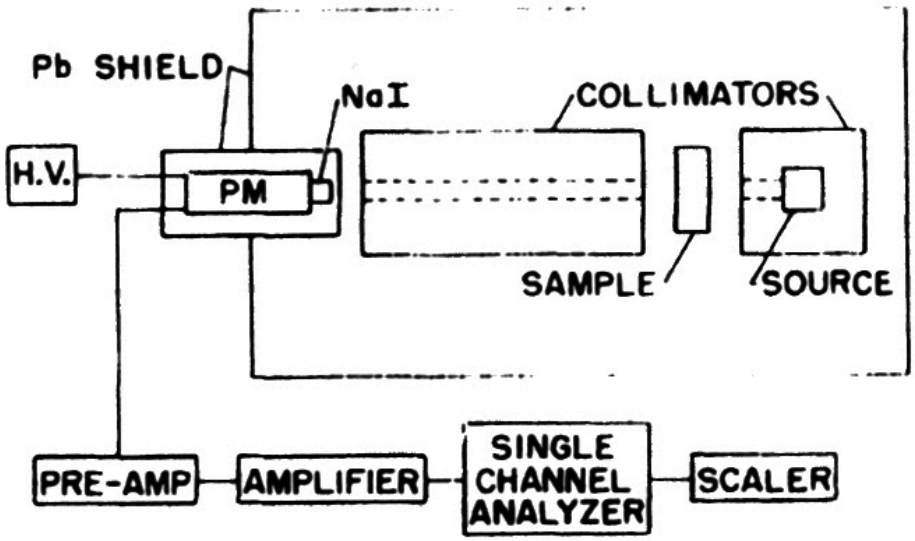

FIG. 1. Schematic diagram of experimental apparatus.

(a) Conner [4]

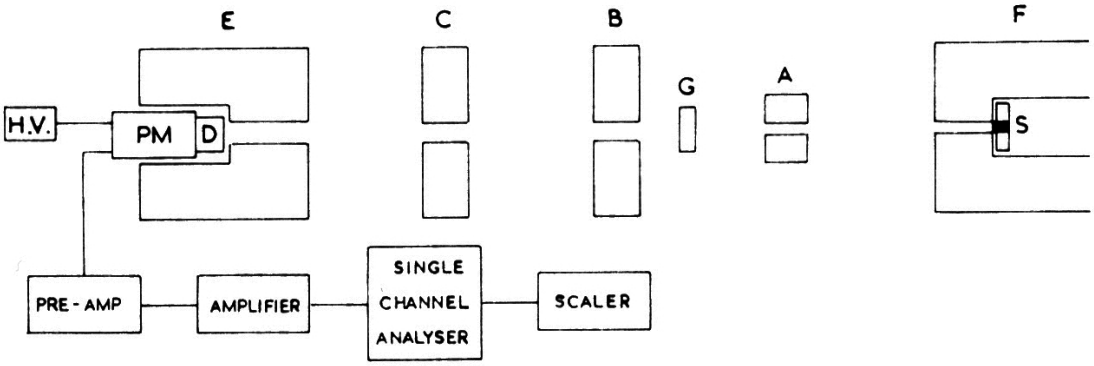

Fig. 1. Schematic diagram of experimental apparatus. S: source in a perspex holder; A: lead collimator (7.5 cm dia long); B and C: lead collimators (30 cm diameter and 7.5 cm long); E and F: lead shielding (30 cm diameter and sample position; D: NaI(Tl) crystal; PM: RCA 6199 photomultiplier; H.V.: high voltage unit.

221

(b) Gopal [9]

Figure 3.1: Experimental apparatii of two previous experimental techniques, A. L. Conner et al.'s paper "Gamma-Ray Attenuation-Coefficient Measurements" from 1970 and Gopal and Sanjeevaiah's paper "A Method to Determine the γ-ray Attenuation Coefficients" from 1973. Both used the Detector $->$ Amplifier $->$ Single Channel Analyzer $->$ Scalar counting system to record the intensities for various thicknesses.

To maximize both the precision and accuracy of the experiments using this equipment a number of measures had to be taken. The single channel scalars were used to discriminate against photons not of interest, but this screening would introduce further errors; a careful preparation of the lab area and selection of photon source mitigated these complications. If the peak of interest from the source was not the highest energy peak, then Compton scattering of higher energy photons would change the background. A non-constant background complicated the analysis. If two photon peaks were close enough (within a few FWHM of each other) complicated curve fitting was required to separate the peaks. Each of these error terms both increased the complexity of the analysis, and more importantly increased the time and complexity of data collection. The effect of this is that at best, the tightest bound of uncertainty for any value directly measured using the equipment and techniques of the era was 3 %, and more realistically, if at least one of the above complications was involved this would increase to 5 %. This is of course without accounting for the uncertainties in geometries that could be controlled, but the experimenters mitigation techniques were not completely detailed in Gopal's methods paper [9].

Single channel analyzers (SCA) were used to select photons of a given energy. Modern multichannel analyzers (MCA) parallelize what would have been done with the single channel devices. With a single channel analyzer and scalar counter the experimenter would first map the peak shape. The experimenter would determine the location, shape, and range usable for the purpose of counting to determine intensity. Additional measurement windows for background subtraction would also need to be determined and measured at each thickness. With these values set, for any given target and source, the regions of interest were measured by using a scalar counter to count the events within the selected range of the SCA, then a repeat measurement on each side of the peak would be made for background subtraction. With a modern MCA and HPGe, the equivalent of hundreds of individual measurements can now be made simultaneously, as one spectrum is recorded for all energies, at a finer resolution than would have been achieved using SCA's. In post-collection analysis these spectra can be mined to determine multiple photon peak intensities for one thickness and the corresponding information needed for background subtraction.

Figure 3.2 shows a comparison of the same ^{133}Ba source measured with a HPGe (red) and a NaI (blue) detector, recorded on the same multi-channel analyzer. On the left side, the shape of the 80 keV peak is much sharper with the HPGe. On the right, with the NaI detector the 303 and 354 keV peaks are visible, but the 383 and 271 keV peaks are completely indistinguishable. While it may not affect the results of this experiment it should also be noted that all detectors suffer from a relative efficiency sensitivity. For photon detectors of these energies, as the energy increases the ability to detect decreases. This is illustrated in the relative measured intensities of the 80 and 356 keV photons. The 80 keV photon has a relative intensity greater than that of the 356 keV photon as seen by the HPGe, even though 356 keV photons are produced from the ^{133}Ba source about twice as frequently.

Figure 3.2 plotted intensity versus energy, but in reality what is measured by the detection equipment is the number of times a pulse of a specific voltage is detected. The original experimenters, being limited by the aforementioned single channel analyzers, would only have been able to isolate individual peak ranges. If they were interested in using the 354 keV peak, they would have set the discrimination window to count pulses that were within the range of the peak shown. By doing so, they would also detect 383 keV photons. While curve separation techniques exist to adjust the

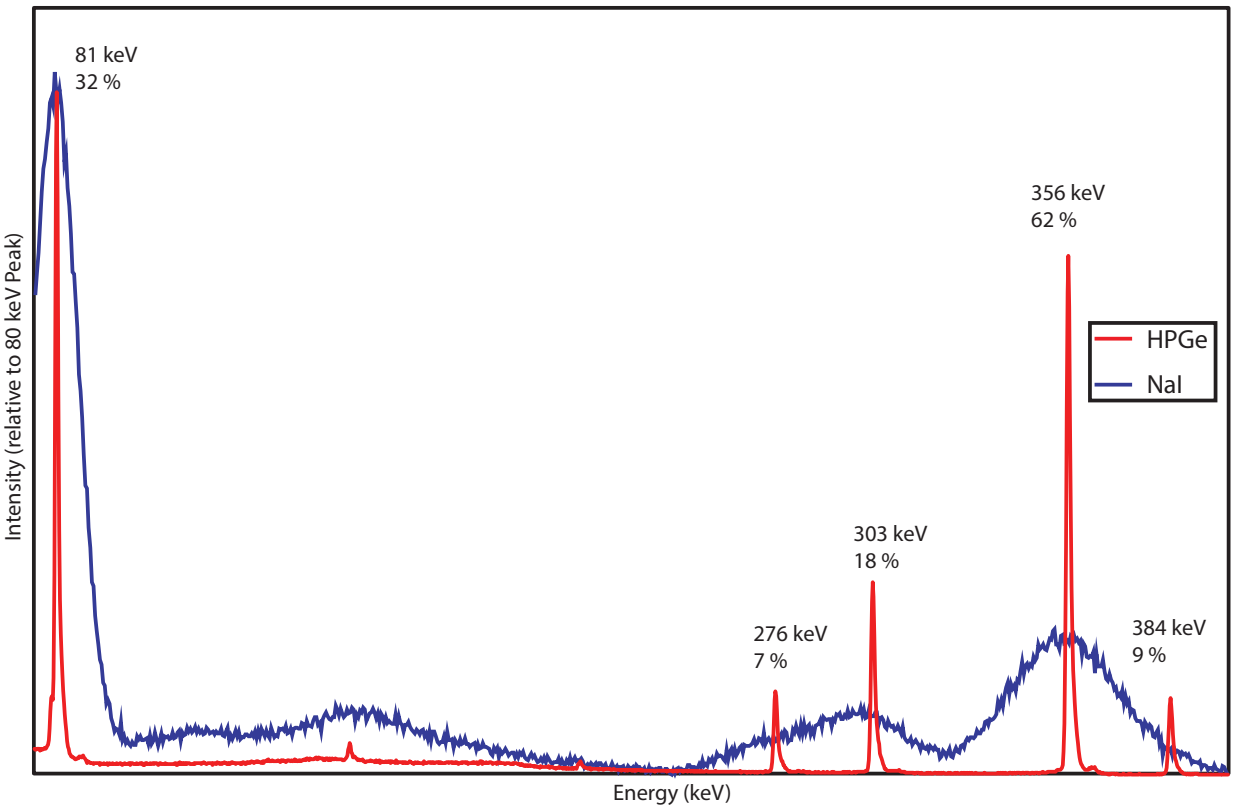

Figure 3.2: Barium-133 spectrum from both a HPGe detector (red) and NaI detector (blue) for the energy range of 75 keV to 400 keV. Each spectrum was individually collected by this author. The improved resolution of the HPGe is advantageous for peak analysis.

data, this would have further increased the uncertainty in the results. If they were interested in picking the 80 keV peak, they would have been unable to fully account for the photons of higher energy that had been Compton scattered and detected. In either case this would lead to uncorrected measurements underestimating the mass attenuation coefficient, or the corrected values could overestimate said values. In either case the uncertainty would be increased further.

These limitations of early equipment are important to understand because most of the values relied upon are calculation based, and normalized to experimental values like those in Gopal and Sanjeevaiah's corresponding data paper "Gamma-Ray Mass Attenuation Coefficients" [10] and Hubbell's "Photon Mass Attenuation and Energy-Absorption Coefficients from 1 keV to 20 MeV" [13]. Scofield outlines the model calculations most commonly relied upon in "Theoretical photoionization cross sections from 1 to 1500 keV" [24], which was used to directly calculate the values for Storm et al. [25]. Further work and resources relied upon today are directly built upon these sources and their conclusions.

CHAPTER 4

EXPERIMENT

As pointed out in Chapter 1 the key motivations for this project are the improvements to accuracy for the total mass attenuation coefficients of the human body to the benefit of health science and diagnostic/treatment medicine techniques. To this end, Table 4.1 shows the key elements of interest, with relative human body contribution by mass.

Element	%
Oxygen	65
Carbon	18
Hydrogen	10
Nitrogen	3
Calcium	1.5
Phosphorus	1.2

Table 4.1: Breakdown of elemental composition of the human body by percent mass composition [2].

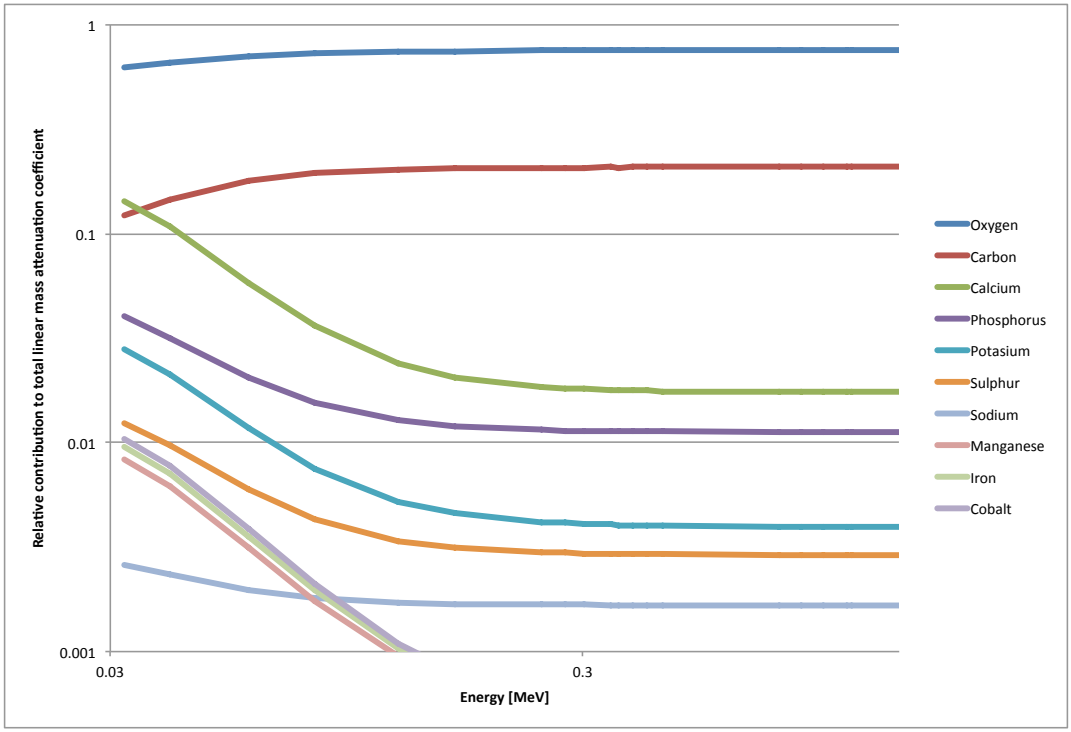

Figure 4.1: Log plot of the relative percent contribution of each element to the total mass attenuation coefficient according to XCOM, for energies ranging from 40 keV to 1.4 MeV.

To understand the relative effect each element has on model calculations for the mass attenuation of a human being, the XCOM values were examined. Figure 4.1 shows the relative contribution, x_i, of each element to the total mass attenuation coefficient based on Table 4.1.

$$x_i(E_\gamma) = \frac{w_i \left(\frac{\mu}{\rho}\right)_i}{\left(\frac{\mu}{\rho}\right)_{\text{total}}} \tag{4.1}$$

where $x_i(E_\gamma)$ is the relative contribution of element i for E_γ and w_i is the relative mass fraction. Figure 4.1 leads to a few predictions, the first being that an approximation based on carbon and oxygen should be within 10 % of the real value. Including calcium and phosphorus should be sufficient to get within 1 % for higher energies. To get within 1 % for all energies of interest adding phosphorus and sulphur is sufficient. To make these claims it is necessary to assume atomic homogeneity, which is of course false — bone's mineral content and density are quite different from that of muscle or fat. Since the values reported here are accurate to 2-5 %, the calculations for bone or muscle based on composition would be on the same order of precision as the applications thereof.

The list of elements of interest to this project are oxygen, carbon, and calcium. Carbon was previously measured in the summer of 2010 by Christine Roh, using the solid method. Neither oxygen or calcium could be measured using the traditional solid method, outlined in Section 4.2, so a new method was needed. The liquid method, Section 4.3, depends on Bragg's Additive Law to calculate the mass attenuation coefficient from mixtures. Water was used to determine the value of oxygen, under the assumption that hydrogen's mass attenuation coefficient can be solved exactly. This is a relatively safe assumption since the energy range involved is entirely Compton-dependant for hydrogen, and single electron solutions require far fewer approximations than for those elements with $Z > 1$. The calcium mass attenuation coefficient was determined by measuring the linear attenuation coefficient of a 10 % solution of hydrated calcium nitrate salt in water and analyzing the corresponding results using Bragg's Additive Law. To test the assumption that Bragg's Additive Law is relevant to this energy range, three metals and corresponding nitrate salt solutions were measured (aluminium, nickel, and copper).

4.1 Sources Used

Four sources were relied upon for various photons. While some sources do emit other photons that might have been detectable, complications surrounding those other photons reduced their usability. Only the following photons for each isotope were analysed

Source	Energy [MeV]
Europium-152	0.040
	0.122
	0.245
	0.344
	0.444
	0.779
	0.867
	0.964
	1.086
	1.112
	1.408
Barium-133	0.081
	0.276
	0.303
	0.356
	0.384
Americium-241	0.060
Cesium-133	0.667

4.2 Solid Targets

For measuring the mass attenuation coefficient of solid targets the detector was mounted horizontally. Thin foils of copper, aluminium (both 0.1 mm), or nickel (0.2 mm) were placed in a custom target holder (seen in red on Figure 4.2a) and the source was placed in a second mount (seen in green). Varying thicknesses of target were achieved by adding more foils. The lead shielding (used to allow for long data collection times) was lined with copper to ensure there was no significant photon contribution from decays within the lead shielding. This setup was chosen for comparability to the previous methods used by Gopal and Sanjeevaiah [9].

(a) Ideal diagram of experiment, top down view

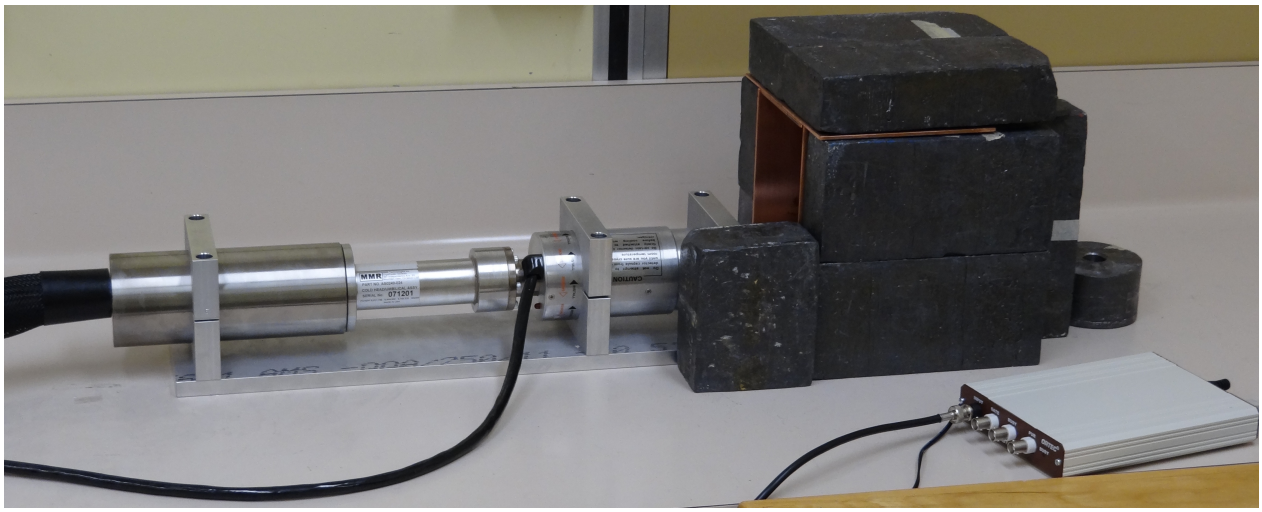

(b) Picture of equipment

Figure 4.2: HPGe detector the horizontal configuration for solid foil target data acquisition.

4.3 Liquid Target

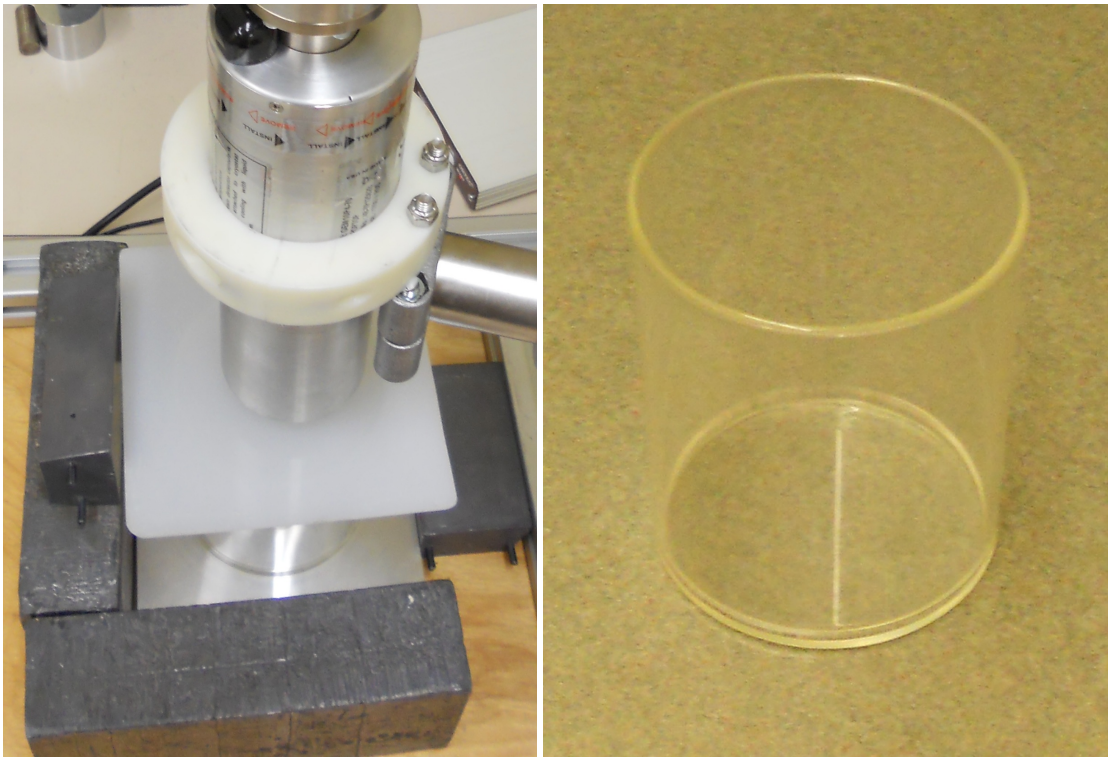

(a) Detector **(b)** Beaker

Figure 4.3: HPGe detector in vertical configuration with beaker and thin plastic cap in data collection configuration.

For measuring the mass attenuation coefficient of liquid media, the detector was mounted in a vertical configuration. The liquid was contained in a beaker between the sources and the detector, as seen in Figure 4.3a. The beaker was made by capping tubing (110 mm wide, < 2 % variance in diameter) with a glass window, seen in Figure 4.3b. The beaker rested on a baseplate and levelled table, ensuring the liquid level remained flat, uniform, and centred with respect to the source. Figure 4.3a shows the base, surrounding lead to minimize exposure to the experimenter when seated at the nearby workstation, and a thin plastic sheet required to reduce evaporation to negligibility. Target solutions were added by mass m to the beaker, and the corresponding thickness, t, was calculated from the beaker's geometry according to

$$t = \frac{m}{\pi r^2 \rho}, \tag{4.2}$$

where r is the radius and ρ is the density. For filtered water ρ was calculated using temperature (24°C corresponds to 0.9997 g/cm^3), and for solutions it was measured using an average of three 50.00±0.05 mL pipette samples. This technique was able to reduce the uncertainty in the thickness to less than 0.1 mm.

4.4 Data Collection

Great care was needed to ensure the integrity of the data. To ensure that all direct measurements could be compared, consistency between measurement methods and timing was wherever possible maintained. When not possible due to the differences in target type, extra care was placed in the determination of additional points of error to ensure that the results maintained comparability. To understand these precautions, this section will describe the general laboratory procedures, then outline the special considerations required for specific target types. All reported uncertainties in this work are two standard deviations, or 95 % confidence intervals.

4.4.1 Solid Target

Sheets of metal were procured through Alfa Aesar, with a uniformity of thickness to better than 5 % relative to the nominal value, which was further refined by repeated measurements with a micrometer. The metallic composition was guaranteed to greater than 99.99 % pure for each of the nickel, copper, and aluminum sheets. From the single sheet of metal a minimum of twenty small foils were cut, ensuring that the size of foils were consistent and that the material did not come into contact with other metals or water, either of which could have introduced errors. The first 20 of the minimum 38 foils each foil's thickness was directly measured at least 5 times per foil using a standard micrometer. The uncertainty in each individual foil's thickness was calculated from the standard deviations of these measurements, and the precision limit of the micrometer. If the standard deviation of the mean values of the first twenty foils was less then the mean of the uncertainties of the first 20 foils, then the nominal average and corresponding standard deviation were used as the values for the remaining foils. If not the remaining foils were also individually measured. Table 4.2 show the relevant thicknesses and densities for each metal used. Uncertainty is calculated as twice the standard deviation.

Metal	average thickness of foil [μ]	density [g/cm^3]
Copper	128 ± 2	8.96
Nickel	257 ± 5	8.908
Aluminum	106 ± 3	2.70

Table 4.2: Thicknesses and densities of the averages for each metal foil type measured using the solid target technique

Data collection was done by positioning the foils in the foil holder (see Figure 4.2a) in their order of measurement. A single spectrum measurement was taken from a single source, with 10 minute live time, with 1 foil. The sources were of sufficient strength that extending the measurement times would yield no reasonable increase in uncertainty. Then the process was repeated for each incrementation of the number of foils. The order was 0, 1, 2, 3, 5, 7, 10, 13, 16, 19, 22, 26, 30, 34, and 38 foils. This order was selected such that there would be close to equal spacing between data points along both the x and y axes of the Ln(Intensity) versus thickness plots. This entire process was then repeated for each of the sources. ^{133}Ba and ^{152}Eu each were run separately, while the ^{241}Am and ^{137}Cs sources were stacked to produce a single spectrum.

4.4.2 Liquid Preparation and Collection

Purity of the prepared liquids was of utmost importance to reduce possible uncertainties to below relevance. To ensure that the uncertainty of the composition of each solution was quantifiable, the water stock used had a purity of better than 10 ppm. As such, the dominant errors for the solutions were in the mass measurements used to calculate their concentrations.

To measure the mass attenuation of water, water was added in 14 increments to the beaker pictured in Section 4.3. Solutions of nitrate salts of nickel, copper and aluminium were prepared to a minimum of 8 % by mass. Intensity versus thickness measurements were repeated for each solution for minimum of 14 thicknesses between 0 cm and 9 cm. Nitrate salts were selected because of their high solubility and dissociativity relative to other aqueous salts. These properties ensure the solution's uniformity, further reducing sources of uncertainty.

The measurement procedure itself involved great care to ensure consistency and mitigation of introduced errors. A thin piece of plastic was placed atop the beaker for all measurements to mitigate evaporation. Each thickness was determined by depositing an aliquot of liquid into the beaker, then calculating the corresponding thickness by using the density and geometry measurements. The density of each solution was determined through a minimum of three 50.00 $\pm$ 0.05 mL pipetted aliquots, from which the mass measurement was averaged to determine the density within 1 % uncertainty. Each measurement was taken by first depositing the solution, then using the ^{152}Eu source, a spectrum was recorded. Additional spectra of ^{133}Ba and ^{137}Cs/^{152}Am were then recorded, maintaining source order. The beaker was then remeasured to ensure that there was no appreciable loss of solution, which was followed with the addition of more solution and repeating the loop of measurements. The spectra recorded in either 10 or 15 minute live time intervals, depending on the solution.

4.5 Sample Data Analysis

Data analysis for this project required multiple stages and software programs due to complexity and file size. The detector outputs individual pulses, measured and recorded by a multi-channel analyzer (spectrum seen in Figure 4.4). The output is stored as a 8192 channel text file. To isolate a single peak, the text file was imported into Microsoft Excel, then a 100-channel group was selected.

This 100-channel group was copied into Mathematica (Figure 4.5) and curve-fit to a gaussian. Mathematica was chosen for this portion because of its ability to re-select data ranges quickly. The peak range to be analyzed was selected such that there were at least 10 flat data points were on each side of the peak to be able to calculate the background.

The peaks were then imported into Matlab (Figure 4.6) to calculate the peak shape. The center point and Full-Width-Half-Max ($FWHM$) were used to determine the area of interest.

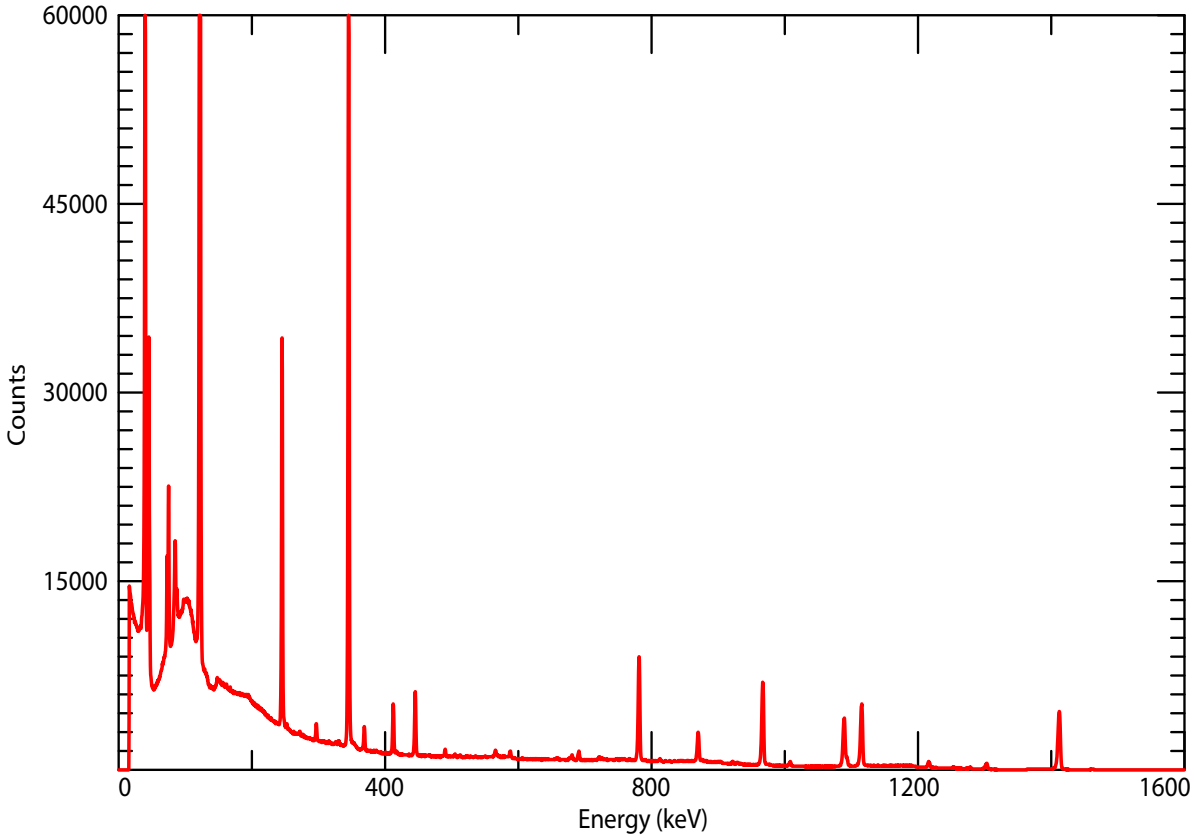

Figure 4.4: Multi-channel analyzer display of europium-152, showing high resolution energy spectrum from 30 to 1600 keV. The energy resolution for the entire region is better than 3 keV. A clear separation of full energy peaks of all photons can be seen.

```
data =
  nlm =
   NonlinearModelFit[data, (a1 Exp[-(x-b1)^2/(2 σ1^2)]), {a1, {b1, 121.58}, σ1}, x];
Show[ListPlot[data], Plot[nlm[x], {x, 115, 125}]]
nlm["ParameterTable"]
```

Out[244]=

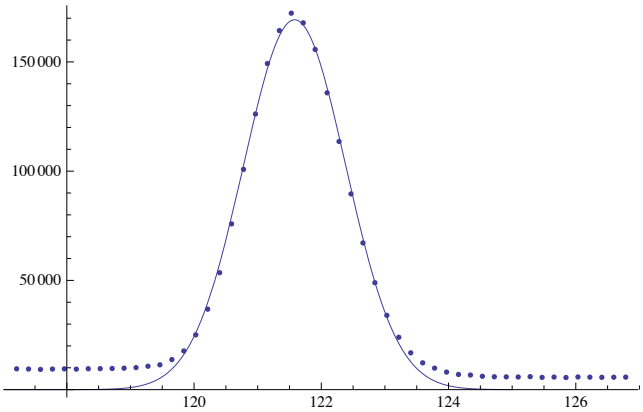

Out[245]=

	Estimate	Standard Error	t-Statistic	P-Value
a1	169290.	2691.95	62.8878	1.60783×10^{-48}
b1	121.58	0.0147377	8249.59	3.62436×10^{-152}
σ1	0.802653	0.0147377	54.4624	1.67792×10^{-45}

Figure 4.5: Mathematica work to select data for one peak. The fit function $(a1Exp[-(x-b1)^2/(2(\sigma1)^2)]$ corresponds to a gaussian $f(x) = ae^{\left(\frac{-(x-b)}{2\varsigma^2}\right)}$ where b is the peak center, and ς is the standard deviation of the gaussian.

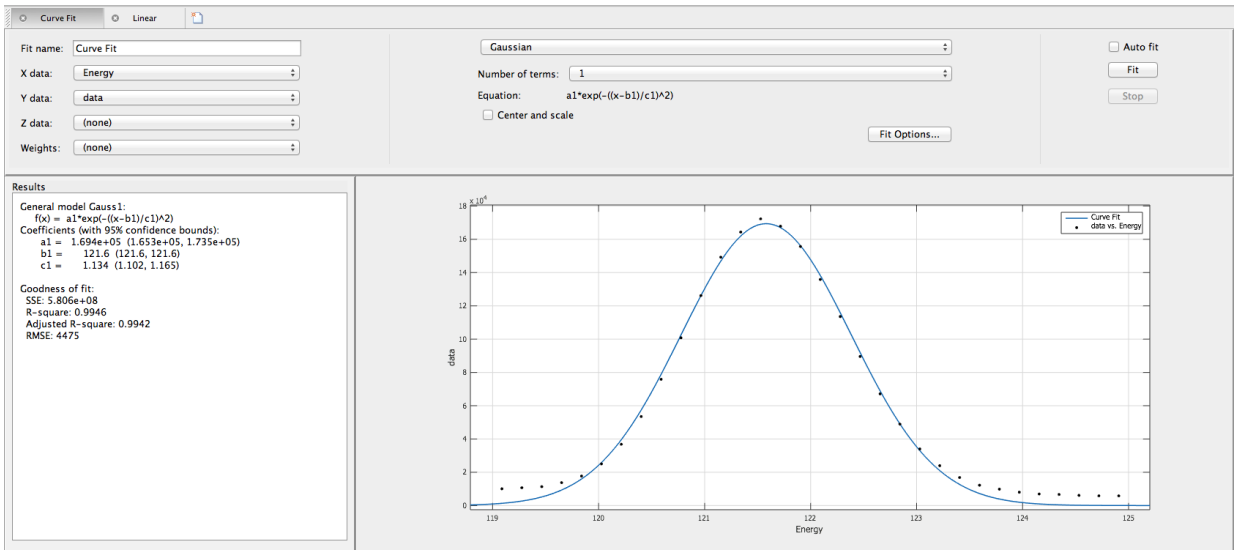

Figure 4.6: Matlab cftool output of a single peak; the left side contains the relevant fit parameters. Coefficient a1 denotes the amplitude, b1 denotes the peak location, and c1 denotes the standard deviation.

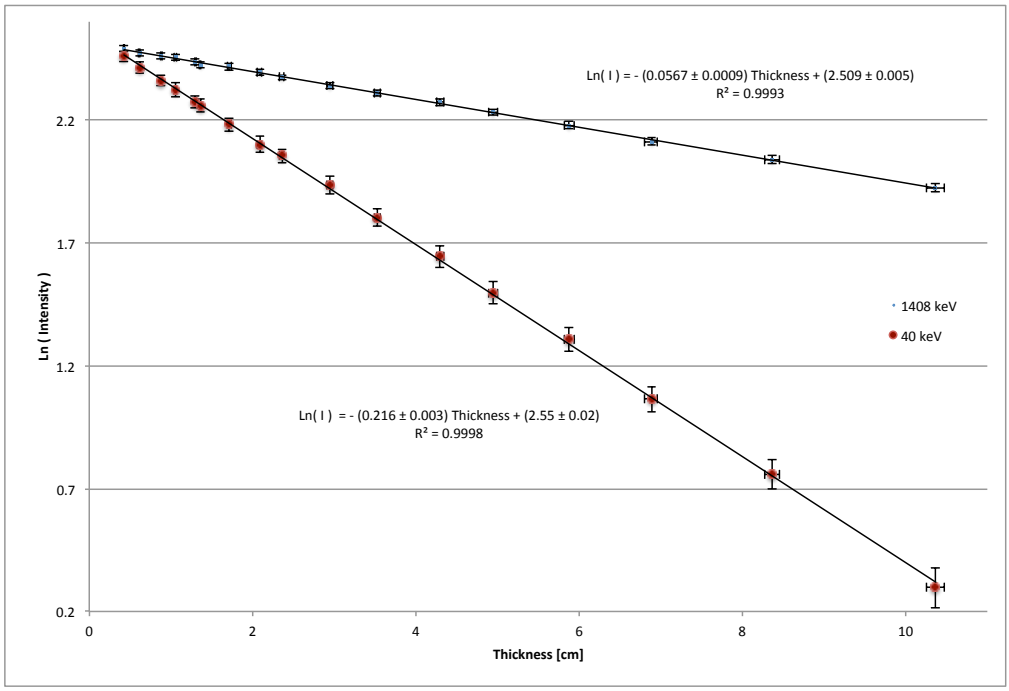

Figure 4.7: Plot of $\ln(I/I_0)+2.5$ versus thickness for various thicknesses of water between 0 cm and 13 cm for the two most disparate photon energies. The 2.5 offset factor is for graphical purposes only. The steep difference in slopes from 40 keV to 1.4 MeV require no additional adjustments to the technique.
The density of water at 24°C was 0.9997 g/cm^3, which was used to calculate the corresponding mass attenuation coefficients from the reported slopes.

The $FWHM$ range was found by

$$FWHM = 2\sqrt{2\ln(2)}\varsigma \tag{4.3}$$

The data was summed over the channels inside the FWHM range, rounding in to create a uncorrected total count of the number of events detected within any peak. To correct for the background, plateaus to either side of the peak are fit; this fit is used to calculate the base count rate under the peak, which is then subtracted from the total count to produce an adjusted event value. To determine the attenuation coefficient the natural log of these event values were plotted against the corresponding thicknesses, as per Equation 4.4, producing Figure 4.7.

$$\ln[I(t)] = -\mu t + \ln[I_0] \tag{4.4}$$

Each slope was calculated using Matlab, then the slope was divided by the density of the target material (and temperature adjusted when necessary) to produce the mass attenuation coefficient for the target.

CHAPTER 5

MEASURED ATTENUATION COEFFICIENTS

The following chapter contains the final measured results of the mass attenuation coefficients for water, the compared salt solutions and reference metal foils. Each value is in units of cm^2/g and all uncertainty values are reported to 2 standard deviations. The values presented here, and some of their implications have been reported at two conferences, the IEEE Nuclear Science Symposium and Medical Imaging Conference (2011) [5] and the 33 Annual CNS/36 Annual CNA Student joint conference (2012) [6].

5.1 Water

Energy [MeV]	XCOM	μ/ρ
0.040	0.2683	0.2161 ± 0.0042
0.060	0.2067	0.1853 ± 0.0028
0.081	0.1829	0.1665 ± 0.0022
0.122	0.1605	0.1467 ± 0.0031
0.245	0.1277	0.1212 ± 0.0018
0.276	0.1224	0.1180 ± 0.0019
0.303	0.1183	0.1130 ± 0.0013
0.344	0.1126	0.1075 ± 0.0015
0.356	0.1111	0.1066 ± 0.0012
0.384	0.108	0.1043 ± 0.0014
0.444	0.1018	0.1002 ± 0.0037
0.663	0.08576	0.0842 ± 0.0035
0.779	0.07963	0.0764 ± 0.0044
0.867	0.07575	0.0736 ± 0.0052
0.964	0.07199	0.0691 ± 0.0017
1.086	0.0679	0.0657 ± 0.0023
1.112	0.0671	0.0637 ± 0.0026
1.408	0.05946	0.0569 ± 0.0020

Table 5.1: Water mass attenuation data, measured at 24°C and adjusted for altitude all uncertainties reported are 2σ

5.2 Liquid Measurements

Energy [MeV]	HNO_3	$Ca(NO_3)_2$	$Al(NO_3)_3$	$Ni(NO_3)_2$	$Cu(NO_3)_2$
0.040	0.21898 ± 0.0026	0.2463 ± 0.0026	0.2086 ± 0.0033	0.28614 ± 0.0058	0.3164 ± 0.002
0.060	0.17341 ± 0.0025	0.1825 ± 0.0021	0.1756 ± 0.0018	0.19523 ± 0.0035	0.2071 ± 0.004
0.081	0.16569 ± 0.0015	0.1647 ± 0.0011	0.1612 ± 0.0009	0.1712 ± 0.0034	0.1705 ± 0.003
0.122	0.14649 ± 0.0006	0.1467 ± 0.0004	0.1474 ± 0.0009	0.1493 ± 0.0029	0.1515 ± 0.002
0.276	0.1158 ± 0.0019	0.1178 ± 0.0014	0.118 ± 0.0011	0.11687 ± 0.0025	0.1118 ± 0.002
0.303	0.11382 ± 0.0004	0.1146 ± 0.0008	0.114 ± 0.0016	0.11282 ± 0.0022	0.1143 ± 0.002
0.356	0.10723 ± 0.0007	0.1077 ± 0.0004	0.1075 ± 0.0007	0.1077 ± 0.002	0.108 ± 0.002
0.384	0.10459 ± 0.0015	0.1049 ± 0.0009	0.1065 ± 0.0012	0.10529 ± 0.0024	0.1057 ± 0.002
0.663			0.0844 ± 0.0013		

Table 5.2: Mass attenuation data of salt solutions and nitric acid, measured at 24°C. All uncertainties are 2σ.

Energy [MeV]	Al (error)	Ni (error)	Cu (error)
0.040	0.51704 ± 0.007	4.4353 ± 0.1274	4.5671 ± 0.1952
0.060	0.27007 ± 0.0167	1.4324 ± 0.0382	1.4318 ± 0.0526
0.081	0.17563 ± 0.0048		0.6977 ± 0.0022
0.122	0.1287 ± 0.0031	0.2694 ± 0.0022	
0.245	0.09574 ± 0.0078		
0.276	0.09093 ± 0.0115		0.1107 ± 0.0026
0.303	0.09089 ± 0.0139		0.1041 ± 0.002
0.344	0.08096 ± 0.0053		
0.356	0.0828 ± 0.010		0.1149 ± 0.0047
0.663		0.0734 ± 0.0045	

Table 5.3: Mass attenuation data of metal foils. All uncertainties are 2σ.

CHAPTER 6

ANALYSIS AND DISCUSSION

This experiment set out to revisit the measurement techniques of mass attenuation coefficients and the usability of Bragg's Additive Law. In this chapter the measurements of water will be explored, then the analysis will expand to use the measured values to show the usability of Bragg's Additive Law and the solution measurement technique.

6.1 Water

If XCOM values are treated as exact then only the 0.444, 0.663, 0.779, and 1.086 MeV photon measurements are within error of the expected reference of XCOM. Since XCOM is model dependant and normalized to measurement data, treating its values as exact is not honest. While XCOM does not provide any uncertainties within its own database, a reading of the papers from which measurement data used in XCOM is based leads to a reasonable lower bound relative 2σ error of 5 % for the energy range of interest (as discussed in Chapter 3). With this uncertainty, the comparison of XCOM and this paper's measurements show all measurements of 0.245 keV or higher photon energy agree. The energies for which the mass attenuation coefficients do not agree can be found in Table 6.1. This disagreement is to be expected since, for oxygen, the energy range in question is dominated by the photo-electric effect, which Section 2.1 already showed to be problematic.

Energy [keV]	XCOM	ΔXCOM	μ/ρ	$\Delta\mu/\rho$	σ difference
40	0.2683	0.0134	0.2161	0.0042	5.9
59.5	0.2067	0.0103	0.1853	0.0028	3.3
81	0.1829	0.0091	0.1665	0.0022	2.9
122	0.1605	0.0080	0.1467	0.0031	2.5

Table 6.1: Comparison of photon energies that do not agree between XCOM and measurement.

6.2 Bragg's Additive Law

Bragg's Additive Law states

$$\left(\frac{\mu}{\rho}\right) = \sum_i w_i \left(\frac{\mu}{\rho}\right)_i \tag{6.1}$$

To find the mass attenuation coefficient for a metal from the measured mass attenuation of a solution the following expansions of Bragg's Additive Law were used.

$$\left(\frac{\mu}{\rho}\right)_{\text{solution}} = \frac{m_{\text{salt}}}{m_{\text{salt}} + m_{\text{H}_2\text{O}}} \left(\frac{\mu}{\rho}\right)_{\text{salt}} + \frac{m_{\text{H}_2\text{O}}}{m_{\text{salt}} + m_{\text{H}_2\text{O}}} \left(\frac{\mu}{\rho}\right)_{\text{H}_2\text{O}} \tag{6.2}$$

$$\left(\frac{\mu}{\rho}\right)_{\text{salt}} = \frac{M_{\text{dry salt}}}{H \times M_{\text{H}_2\text{O}} + M_{\text{dry salt}}} \left(\frac{\mu}{\rho}\right)_{\text{dry salt}} + \frac{H \times M_{\text{H}_2\text{O}}}{H \times M_{\text{H}_2\text{O}} + M_{\text{dry salt}}} \left(\frac{\mu}{\rho}\right)_{\text{dry salt}} \tag{6.3}$$

$$\left(\frac{\mu}{\rho}\right)_{\text{dry salt}} = \frac{M_{\text{metal}}}{M_{\text{dry salt}}} \left(\frac{\mu}{\rho}\right)_{\text{metal}} + \frac{N \times M_{\text{NO}_3}}{M_{\text{dry salt}}} \left(\frac{\mu}{\rho}\right)_{\text{NO}_3} \tag{6.4}$$

Where m_i is the measured mass, in grams, of i and M_i is the Molar Mass of i. The factors N and H represent the nitration, and hydration factors, respectively. The nitration factor is the number of NO_3 groups attached to each metal atom when in crystalline form and the hydration factor is the number of H_2O molecules per salt molecule suspended in the crystal lattice. The subscript dry salt signifies the properties of the anhydrous form of the salt.

The set of above equations can be rewritten in terms of $\left(\frac{\mu}{\rho}\right)_{\text{metal}}$

$$\begin{aligned}\left(\frac{\mu}{\rho}\right)_{\text{metal}} = \frac{1}{M_{\text{metal}} m_{\text{salt}}} \Bigg[& \left(\frac{\mu}{\rho}\right)_{\text{solution}} \left(m_{\text{salt}} + m_{\text{H}_2\text{O}}\right)\left(M_{\text{dry salt}} + H \times M_{\text{H}_2\text{O}}\right) \\ & - \left(\frac{\mu}{\rho}\right)_{\text{NO}_3} \left(N \times M_{\text{NO}_3} m_{\text{salt}}\right) \\ & - \left(\frac{\mu}{\rho}\right)_{\text{H}_2\text{O}} \left(M_{\text{dry salt}} m_{\text{H}_2\text{O}} + H \times M_{\text{H}_2\text{O}} \left(m_{\text{salt}} + m_{\text{H}_2\text{O}}\right)\right) \Bigg]\end{aligned} \tag{6.5}$$

where $\left(\frac{\mu}{\rho}\right)_{\text{metal}}$ is, with the exception of $\left(\frac{\mu}{\rho}\right)_{\text{NO}_3}$, written entirely in terms of quantities: either measured in-lab as part of solution preparation $(m_{\text{H}_2\text{O}}, m_{\text{salt}})$, measured using liquid mass attenuation techniques $\left(\left(\frac{\mu}{\rho}\right)_{\text{solution}}, \left(\frac{\mu}{\rho}\right)_{\text{H}_2\text{O}}\right)$, a property of the salt (N, H), or the molar masses calculated from data provided by the International Union of Atomic Weights and Measures' atomic weights workgroup.

$\left(\frac{\mu}{\rho}\right)_{NO_3}$ can be similarly found from

$$\left(\frac{\mu}{\rho}\right)_{HNO_3} = \frac{M_H}{M_{HNO_3}}\left(\frac{\mu}{\rho}\right)_H + \frac{M_{NO_3}}{M_{HNO_3}}\left(\frac{\mu}{\rho}\right)_{NO_3} \tag{6.6}$$

$$\left(\frac{\mu}{\rho}\right)_{acid} = \frac{m_{HNO_3}}{m_{HNO_3}+m_{H_2O}}\left(\frac{\mu}{\rho}\right)_{HNO_3} + \frac{m_{H_2O}}{m_{HNO_3}+m_{H_2O}}\left(\frac{\mu}{\rho}\right)_{H_2O} \tag{6.7}$$

rewritten in the form

$$\left(\frac{\mu}{\rho}\right)_{NO_3} = \frac{1}{m_{HNO_3}M_{NO_3}}\left[\left(\frac{\mu}{\rho}\right)_{acid} M_{HNO_3}\left(m_{H_2O}+m_{HNO_3}\right) - \left(\frac{\mu}{\rho}\right)_H \left(M_H m_{HNO_3}\right) - \left(\frac{\mu}{\rho}\right)_{H_2O}\left(M_{HNO_3}m_{H_2O}\right)\right] \tag{6.8}$$

6.2.1 Copper

If we take the case of copper and its nitrate salt, $Cu(NO_3)_2{\cdot}2.5\ H_2O$ then the above equation can be simplified using the values listed in Table 6.2. Since the relative uncertainties are all less than 0.01 % (shown in brackets) these values will be treated as exact.

M_i	Formula	Value (uncertainty) [g/mol]
metal	Cu	63.546 (0.001)
dry salt	$Cu(NO_3)_2$	187.554 (0.009)
salt	$Cu(NO_3)_2{\cdot}2.5\ H_2O$	232.592 (0.018)
	NO_3	62.004 (0.004)
	H_2O	18.015 (0.003)

Table 6.2: List of values with uncertainties for the molar masses needed to evaluate Equation 6.5 for copper(II)nitrate.

Equation 6.5 simplifies to

$$\left(\frac{\mu}{\rho}\right)_{metal} = 3.66021\frac{m_{H_2O}}{m_{salt}}\left(\left(\frac{\mu}{\rho}\right)_{solution} - \left(\frac{\mu}{\rho}\right)_{H_2O}\right) + - 1.95147\left(\frac{\mu}{\rho}\right)_{NO_3} + 3.66021\left(\frac{\mu}{\rho}\right)_{solution} - 0.708739\left(\frac{\mu}{\rho}\right)_{H_2O} \tag{6.9}$$

accurate to five significant figures. The uncertainty correspondingly simplifies to

$$\begin{aligned}\delta\left(\frac{\mu}{\rho}\right)_{\text{metal}} =& 3.66021\frac{m_{H_2O}}{m_{\text{salt}}}\left(\delta\left(\frac{\mu}{\rho}\right)_{\text{solution}}+\delta\left(\frac{\mu}{\rho}\right)_{H_2O}\right)+\\ & 3.66201\frac{m_{\text{salt}}\delta m_{H_2O}+m_{H_2O}\delta m_{\text{salt}}}{m_{\text{salt}}^2}\left(\left(\frac{\mu}{\rho}\right)_{\text{solution}}-\left(\frac{\mu}{\rho}\right)_{H_2O}\right)+\\ & +1.95147\,\delta\left(\frac{\mu}{\rho}\right)_{NO_3}+3.66021\,\delta\left(\frac{\mu}{\rho}\right)_{\text{solution}}+0.708739\,\delta\left(\frac{\mu}{\rho}\right)_{H_2O}\end{aligned} \tag{6.10}$$

6.2.2 Results and Comparison

The mass attenuation coefficients found using Bragg's Additive Law are compared with direct measurements of metal foils for both copper and nickel in Table 6.3. All measured and calculated values shown are in agreement, supporting the validity of Bragg's Additive Law, and the liquid dissolved salt method can be used to find mass attenuation coefficients.

Energy	Copper [cm^2/g]		Nickel [cm^2/g]	
[keV]	Derived	Measured	Derived	Measured
40	4.32 ± 0.35	4.57 ± 0.20	4.71 ± 0.76	4.44 ± 0.13
59.5	1.30 ± 0.34	1.43 ± 0.05	1.07 ± 0.49	1.43 ± 0.04

Table 6.3: Photon mass attenuation values for direct measurement of metal and derived from measurements of the corresponding metal nitrate salt using Bragg's Additive Law (Equation 6.5 and Equation 6.8)

Further analysis of the uncertainties in Table 6.3 will be discussed in Section 6.3. Section 1.2 showed that calcium is the most significant metal to the mass attenuation coefficient of the human body. For the energies of 40 and 59.5 keV the mass attenuation coefficient values calculated using Bragg's Additive Law and the liquid attenuation measurement technique are shown in Table 6.4

Energy	Ca
[keV]	[cm^2/g]
40	1.93 ± 0.57

Table 6.4: Photon mass attenuation values for calcium, calculated using Bragg's Additive Law. Linear attenuation coefficients for the measured solution for higher energies were indiscernible from deionized water, and thus were not analyzed.

6.3 Uncertainty Analysis

The ability to further reduce uncertainties beyond those presented here are problematic. For comparison purposes nitrate salts were chosen for two properties: solubility and consistency. The greater the solubility the higher the concentration of metal ions and the greater the energy range the technique can be used for. Nitrate salts have one problem in that they are in general hydrous crystals. The hydration factor multiplies the original water measurement's effect on uncertainty. To remove the hydration groups from the salt the least impactful method is to bake the water out. For some salts, including those used in this experiment, the temperature required to bake the water out would be enough to drive oxygen atoms out of the nitrates. This change in chemistry would both change the solubility and introduce uncertainty into the stoichiometric ratios of the solution. To overcome this problem a case by case selection of metal salt selecting low hydration factors and high solubility would allow for greater precision.

The ability to reduce the two error factors of thickness of target and statistical uncertainty are linked. Using the sources provided the highest source event detection rate was on the order of 12000 cts/sec. Even at this detection rate to get peaks with sufficient statistics for analysis individual measurement times were on the order of 10 to 15 minutes. To reduce the relative error in the peak intensities by a factor of two would require quadrupling the runtime. Such a long runtime would mean that evaporation over the course of 40 minutes per measurement would be significant and the uncertainties would need to be adjusted. This quickly approaches a limit of diminishing returns, where any decrease in statistical uncertainty would be met with a larger increase in thickness uncertainty. A new beaker design able to better mitigate evaporation would be necessary to extend measurement times any longer than used in this experiment.

6.3.1 Error Equations

Nitrate

The the mass attenuation coefficient for nitrate is dictated by

$$\left(\frac{\mu}{\rho}\right)_{NO_3} = \frac{1}{m_{HNO_3} M_{NO_3}} \left[\left(\frac{\mu}{\rho}\right)_{acid} M_{HNO_3} \left(m_{H_2O} + m_{HNO_3}\right) - \left(\frac{\mu}{\rho}\right)_{H} \left(M_H m_{HNO_3}\right) - \left(\frac{\mu}{\rho}\right)_{H_2O} \left(M_{HNO_3} m_{H_2O}\right) \right] \tag{6.11}$$

the corresponding uncertainty, written in the most general form and grouped as a linear expression with respect to contributing measurement uncertainties is

$$\begin{aligned}\delta\left(\frac{\mu}{\rho}\right)_{NO_3} &= \delta\left(\frac{\mu}{\rho}\right)_{\text{acid}}\left(\frac{m_{HNO_3}^2 M_{HNO_3} + m_{HNO_3} M_{HNO_3} m_{H_2O}}{m_{HNO_3}^2 M_{NO_3}}\right) \\ &+ \delta\left(\frac{\mu}{\rho}\right)_{H}\left(\frac{M_H}{M_{NO_3}}\right) \\ &+ \delta\left(\frac{\mu}{\rho}\right)_{H_2O}\left(\frac{M_{HNO_3} m_{H_2O}}{M_{NO_3} m_{HNO_3}}\right) \\ &+ \delta m_{HNO_3}\left(\frac{2 m_{HNO_3} M_{HNO_3}\left(\frac{\mu}{\rho}\right)_{\text{acid}} + M_{HNO_3} m_{H_2O}\left(\frac{\mu}{\rho}\right)_{\text{acid}} + M_{HNO_3} m_{H_2O}\left(\frac{\mu}{\rho}\right)_{H_2O}}{M_{NO_3} m_{HNO_3}^2}\right) \\ &+ \delta m_{H_2O}\left(\frac{m_{HNO_3} M_{HNO_3}\left(\frac{\mu}{\rho}\right)_{\text{acid}} + m_{HNO_3} M_{HNO_3}\left(\frac{\mu}{\rho}\right)_{H_2O}}{m_{HNO_3}^2 M_{NO_3}}\right)\end{aligned} \tag{6.12}$$

Which can be simplified and approximated in terms of the acid strength by

$$\delta\left(\frac{\mu}{\rho}\right)_{NO_3} = \left(\frac{\mu}{\rho}\right)_{H_2O}\left(9.08179\frac{\delta\left(\frac{\mu}{\rho}\right)_{\text{acid}}}{\left(\frac{\mu}{\rho}\right)_{\text{acid}}} + 8.06553\frac{\delta\left(\frac{\mu}{\rho}\right)_{H_2O}}{\left(\frac{\mu}{\rho}\right)_{H_2O}} + 18.08\frac{\delta C}{C}\right) \tag{6.13}$$

where C is the molar concentration of the acid. From this we can create relative impact factors for each uncertainty in each measurement measurement. The impact factor multiplied by the relative error will show which uncertainties have the greatest effect on the uncertainty of $\left(\frac{\mu}{\rho}\right)_{NO_3}$

Uncertainty	Impact factor	typical relative uncertainty	typical contribution to total uncertainty
$\delta\left(\frac{\mu}{\rho}\right)_{\text{acid}}$	0.257	0.04	0.418
$\delta\left(\frac{\mu}{\rho}\right)_{H_2O}$	0.229	0.04	0.372
δC	0.513	0.01	0.209

Table 6.5: Impact factor for each of the uncertainties in the measurements required to determine the mass attenuation coefficient of nitrate. Typical contribution is normalized such that the sum of all constituents is 1. The uncertainty in the measurement of the mass attenuation coefficient will typically have the highest contribution to the uncertainty in the mass attenuation coefficient of NO_3

There are two important pieces of information that the above table gives us in reducing the total uncertainty, first that the most impactful source of error is the concentration, and second, that the most significant source of error is the uncertainty in the acid.

If we expand this to Equation 6.5, Table 6.6 shows the resulting impact factors for copper.

Table 6.6 shows that the relative uncertainty of hydrogen would need to be at least four orders of magnitude greater than that of any other data to be relevant. By multiplying the impact factors with the typical relative uncertainties achieved in this work we can see which errors are of greatest importance

Uncertainty	impact factor
δm_{salt}	0.3448
δm_{H_2O}	0.3134
$\delta \left(\frac{\mu}{\rho}\right)_{\text{solution}}$	0.1723
$\delta \left(\frac{\mu}{\rho}\right)_{H_2O}$	0.1629
$\delta \left(\frac{\mu}{\rho}\right)_{\text{acid}}$	0.0032
$\delta \left(\frac{\mu}{\rho}\right)_{H}$	5.7×10^{-6}
δC	0.0032

Table 6.6: The impact factors for each of the uncertainties in each measurement needed to determine the mass attenuation of copper from the direct measurements of each of the above variables. For the contribution of the uncertainty in the mass attenuation of hydrogen to be significant, the relative uncertainties in each of the other measurements would need to be three to five orders of magnitude smaller than that of $\left(\frac{\mu}{\rho}\right)_{H}$.

Uncertainty	impact factor	typical relative uncertainty	typical contribution to total uncertainty
δm_{salt}	0.3448	0.002	0.0481
δm_{H_2O}	0.3134	0.0002	0.0044
$\delta \left(\frac{\mu}{\rho}\right)_{\text{solution}}$	0.1723	0.04	0.4813
$\delta \left(\frac{\mu}{\rho}\right)_{H_2O}$	0.1629	0.04	0.4550
$\delta \left(\frac{\mu}{\rho}\right)_{\text{acid}}$	0.0032	0.04	0.0090
$\delta \left(\frac{\mu}{\rho}\right)_{H}$	5.7×10^{-6}	0.01	0.0000
δC	0.0032	0.01	0.0022

Table 6.7: Typical relative uncertainty and the corresponding normalized contribution (sum of all contributions $\equiv 1$) to the uncertainty in $\left(\frac{\mu}{\rho}\right)_{Cu}$. The two most significant contributions are the error in the mass attenuations of the salt solution and of water.

Uncertainty	impact factor	typical relative uncertainty	typical contribution to total uncertainty
δm_{salt}	0.3448	0.002	0.0481
δm_{H_2O}	0.3135	0.0002	0.0044
$\delta \left(\frac{\mu}{\rho}\right)_{\text{solution}}$	0.1724	0.04	0.4806
$\delta \left(\frac{\mu}{\rho}\right)_{H_2O}$	0.1646	0.04	0.4589
$\delta \left(\frac{\mu}{\rho}\right)_{\text{acid}}$	0.0023	0.04	0.0064
$\delta \left(\frac{\mu}{\rho}\right)_{H}$	4.1×10^{-6}	0.01	0.0000
δC	0.0023	0.01	0.0016

Table 6.8: Typical relative uncertainty and the corresponding normalized contribution (sum of all contributions $\equiv 1$) to the uncertainty in $\left(\frac{\mu}{\rho}\right)_{Ni}$. The two significant contributions are the error the mass attenuations of the salt solution, and water. Notice a slight increase in the total contribution from the uncertainty in the mass attenuation coefficient of water when compared to Table 6.7, due to the higher hydration factor

From Table 6.7 and Table 6.8 we can see that over 90% of the uncertainty is due to the relative errors in the mass attenuation coefficients. This shows that the uncertainty in the Bragg method for measuring the attenuation coefficient of a metal is limited by the experimenter's ability to measure the attenuation coefficients of water and the corresponding solution. To reduce the uncertainties to the point that they were dependant on factors other than the measured mass attenuation coefficients one would need to measure the mass attenuation coefficients to at least an order of magnitude higher precision. Re-evaluating copper with these uncertainties yielded $\left(\frac{\mu}{\rho}\right)_{\text{Cu}} = 4.3197 \pm 0.018$. This would require a reduction in the relative uncertainty of both the thickness and intensity by an order of magnitude. To decrease the uncertainty in the thickness of the solution a number of techniques could be used. If a table of sufficiently level grade could be found (the one used for this experiment was most likely close) an optical measurement system could be constructed, accurate to 100 nm. This would remove the uncertainty due to the beaker's inner diameter from affecting the total uncertainty.

6.4 Refining XCOM

To better refine XCOM, one must be able to determine an uncertainty in the value in a repeatable way. One potential method would be to use the energy resolution limit to determine an appropriate corresponding range for XCOM. When we consider copper, for the 59.5409±0.0001 keV ^{241}Amphoton [21], the detector's FWHM resolution is 2 keV. So for the range of 58.5 to 60.5 keV, XCOM reports a range of 1.704 to 1.558 cm^2/g for the photon mass attenuation coefficient, corresponding to 8.5 % relative error; which is greater than the error supposed in earlier parts of this discussion. If instead we bind ourselves to the precision of XCOM (four significant figures in energy) and assume that the only uncertainty in a photon's energy is due to rounding, then the corresponding range would be 1.626-1.625 cm^2/g. Neither of these seem to estimate a reasonable error for the mass attenuation coefficient. Instead, if we assume that over a small enough energy range the mass attenuation coefficient may be modelled as a linear function (Section B.2), then an interpolation of the fit can provide an uncertainty measure. For fitting to the range of 59.49 to 59.59 keV, the resulting fit is $\left(\frac{\mu}{\rho}\right)_{\text{Cu}}(59.54 \text{ keV}) = 1.63 \pm 0.20$ cm^2/g. This indicates that to determine the error for any value in XCOM a small selection of values needs to be fitted and interpolated. This data suggests a range of $\pm$ 5 in the last significant digit (or fourth significant digit as XCOM limits all entries to no greater than 4 significant figure precision).

6.5 Future Work

To be able to measure calcium over the range of 40 keV to 2 MeV, for which this experiment first set out to accomplish, the liquid target method and apparatus need to be refined such that the measurement uncertainty is reduced by an order of magnitude. To accomplish this a careful selection of highly aqueous salts and standards could be used. Furthermore the beaker needs to be modified to reduce evaporation without impacting on the detection ability. An increase of thickness range of the target would also be required, however doing so would mean that the reintroduction of collimation would be needed since the rate of scattered photons not able to be discriminated against due to frequency shift (shallow Compton scattering) would be significant.

CHAPTER 7

CONCLUSIONS

This project set out to accomplish a number of goals. To test the validity of Bragg's Additive Law, to test the usability and accuracy of the XCOM database, and to come up with direct measurements of interest to medical applications. To do this a new measurement procedure relying on modern technologies was created.

The liquid target measurement technique measured mass attenuation coefficients for both water and for dissolved salt solutions to within a reasonable uncertainty. The execution of this technique displayed two key conclusions. Bragg's law can be used to calculate the mass attenuation coefficient of a constituent from a collection of measurements and the resulting uncertainty from this technique maintains a reasonable uncertainty. The conclusions that can be drawn from this are that for materials that are not easily directly measured, if a soluble salt can be found, the liquid technique can be used to determine that material's photon mass attenuation coefficient for energies which are dominated by photoelectric effect photon-electron interactions.

Comparing the results from this experiment to the current primary reference source, XCOM, show XCOM's discrepancies which are most severe in the photo-electric effect dominant region. The most important element and energy for medical imaging are oxygen and 144 keV (^{99m}Tc) respectively. For applications to medical imaging direct measurements of the photons of interest with water, and other elements; and ^{99m}Tcnew measurements must be made for the specific applications needed. Other photons of interest to medical imaging could be approximated from one of the various measurements reported in Chapter 5, including ^{131}I's 362 keV photon for which this work showed a photon mass attenuation coefficient of 0.1066 ± 0.0012 cm^2/g at 0.356 keV.

XCOM has traditionally reported its values to 4 significant figures without reported uncertainties. Reporting in this way has led the users of these values to assume insignificant uncertainty. An exploration of the inherent precision in XCOM lead to the conclusion that a model fit of $\pm$ 5 in the last significant figure, about the photon energy and material of interest can be used to calculate the intrinsic uncertainty in XCOM.

REFERENCES

[1] A. Akar, H. Baltas, U. Cevik, F. Korkmaz, N. Okumusoglu. Measurement of attenuation coefficients for bone, muscle, fat and water at 140, 364 and 662 keV γ-ray energies. *Journal of Quantitative Spectroscopy and Radiative Transfer*, 102(2):203 – 211, 2006.

[2] R. Chang. *Chemistry*. McGraw-Hill, wydanie 9th, Mar 2006.

[3] A. H. Compton. A quantum theory of the scattering of x-rays by light elements. *Phys. Rev.*, 21:483–502, May 1923.

[4] A. L. Conner, H. F. Atwater, E. H. Plassmann, J. H. McCrary. Gamma-Ray Attenuation-Coefficient Measurements. *Phys. Rev. A*, 1(3):539–544, Mar 1970.

[5] C. Crewson, C. Rangacharyulu. High resolution measuremetns of mass attenuation coefficients for photon energies of 40 kev to 1.4 mev. *Confernence Record for the IEEE Nuclear Science Symposium and Medical Imaging Conference, and the 18th International Workshop on Room-Temperature Semiconductor X-Ray and Gamma Detectors*, Valencia, Spain, 2011. The Institute of Electrical and Electronic Engineers.

[6] C. Crewson, C. Rangacharyulu. Photon mass attenuation coefficients of importance to dosimetry. *Building on our Past, Building for the Future, Conference record for the 33rd Annual Canadian Nuclear Society Conference and 36th Annual CNS/CNA Student Conference*, Saskatoon, Saskatchewan, 2012. Canadian Nuclear Association and Canadian Nuclear Society.

[7] A. Einstein. Über einen die erzeugung und verwandlung des lichtes betreffenden heuristischen gesichtspunkt. *Annalen der Physik*, 17(6):132–148, June 1905.

[8] A. Einstein. *The Collected Papers of Albert Einstein, Volume 2: The Swiss Years: Writings, 1900-1909*. Prinston University Press, 1990.

[9] S. Gopal, B. Sanjeevaiah. A Method to Determine the γ-ray Attenuation Coefficients. *Nucl Inst and Methods*, 107:221–225, 1973.

[10] S. Gopal, B. Sanjeevaiah. Gamma-Ray Attenuation Coefficient Measurements. *Phys. Rev. A*, 8(6):2814–2818, Dec 1973.

[11] J. Hubbell. Photon cross sections, attenuation coefficients, and energy absorption coefficiencts from 10 kev to 100 gev. *National Standards Reference Data Series*, 29, August 1969.

[12] J. Hubbell. Survey of photon-attenuation-coefficient measurements 10 eV to 100 GeV. *Atomic Data and Nuclear Data Tables*, 3:241 – 297, 1971.

[13] J. Hubbell. Photon mass attenuation and energy-absorption coefficients from 1 keV to 20 MeV. *International Journal of Applied Radiation and Isotopes*, 33(11):1269–1290, 1982. cited By (since 1996) 502.

[14] J. H. Hubbell, H. A. Gimm, I. Overbo. Pair, triplet, and total atomic cross sections (and mass attenuation coefficients) for 1 mev-100 gev photons in elements z=1 to 100. *Journal of Physical and Chemical Reference Data*, 9(4):1023–1148, 1980.

[15] J. H. Hubbell, W. J. Veigele, E. A. Briggs, R. T. Brown, D. T. Cromer, R. J. Howerton. Atomic form factors, incoherent scattering functions, and photon scattering cross sections. *Journal of Physical and Chemical Reference Data*, 4(3):471–538, 1975.

[16] International Commission on Radiation Units and Measurements. *Tissue Substitutes in Radiation Dosimetry and Measurements*, wolumen 44. International Commission on Radiation Units and Measurements, 1989.

[17] J. Joseph, F. Rohrlich. Pair production and bremsstrahlung in the field of free and bound electrons. *Rev. Mod. Phys.*, 30:354–368, Apr 1958.

[18] B. Kerur, M. Lagare, R. Nathuram. Non-validity of bragg's additivity law for rare-earth compounds. *Radiation Physics and Chemistry*, 75(1):7 – 13, 2006.

[19] B. Kerur, S. Thontadarya, B. Hanumaiah. A study on the range of non-validity of the bragg's additivity law for compounds at photon energies below 10 kev. *International Journal of Radiation Applications and Instrumentation. Part A. Applied Radiation and Isotopes*, 43(7):893 – 898, 1992.

[20] G. F. Knoll. *Radiation Detection and Measurement*. John Wiley and Sons, wydanie 3rd, 2000.

[21] National Nuclear Data Center. Interactive chart of the nuclides. http://www.nndc.bnl.gov/chart/.

[22] NIST. XCOM photon cross section database, 2009. http://physics.nist.gov/PhysRefData /Xcom/html/xcom1.html.

[23] Particle Data Group. *Journal of Physics G - Review of Particle Physics*, wolumen 37. IOP Publishing, July 2010.

[24] J. H. Scofield. Theoretical photoionization cross sections from 1 to 1500 keV. Technical report, Lawrence Livermore National Laboratory, 1973.

[25] L. Storm, H. I. Israel. Photon cross sections from 1 keV to 100 MeV for elements Z=1 to Z=100. *Atomic Data and Nuclear Data Tables*, 7(6):565 – 681, 1970.

[26] World Nuclear Organization. Radio isotopes in medicine. http://www.world-nuclear.org/info/inf55.html.

APPENDIX A

APPROXIMATIONS

A.1 Limits of the Klein-Nishina formula

$$\frac{d\sigma_{K-N}}{d\Omega} = Zr_0^2 \left(\frac{1}{1+\alpha(1-\cos\theta)}\right)^2 \left(\frac{1+\cos^2\theta}{2}\right) \left(1+\frac{\alpha^2(1-\cos\theta)^2}{(1+\cos^2\theta)(1+\alpha(1-\cos\theta))}\right) \tag{A.1}$$

For the Klein-Nishina formula, $\frac{d\sigma_{K-N}}{d\Omega}$, there are two limits of interest. The cases of $E_\gamma \to 0, \infty$.
Since

$$\alpha = \frac{E_\gamma}{m_0 c^2}$$

the corresponding limits in terms of α are $\alpha \to 0, \infty$.

A.1.1 $\alpha \to 0$

$$\lim_{\alpha\to 0} \frac{d\sigma_{K-N}}{d\Omega} = Zr_0^2 \left(\frac{1+\cos^2\theta}{2}\right) \cdot \lim_{\alpha\to 0} \left[\left(\frac{1}{1+\alpha(1-\cos\theta)}\right)^2 \left(1+\frac{\alpha^2(1-\cos\theta)^2}{(1+\cos^2\theta)(1+\alpha(1-\cos\theta))}\right)\right]$$

Substituting 0 for α

$$\begin{aligned}
&\lim_{\alpha\to 0} \left(\frac{1}{1+\alpha(1-\cos\theta)}\right)^2 \left(1+\frac{\alpha^2(1-\cos\theta)^2}{(1+\cos^2\theta)(1+\alpha(1-\cos\theta))}\right) \\
&= \left(\frac{1}{1+0(1-\cos\theta)}\right)^2 \left(1+\frac{0^2(1-\cos\theta)^2}{(1+\cos^2\theta)(1+0(1-\cos\theta))}\right) \\
&= \left(\frac{1}{1}\right)^2 (1) \\
&= 1
\end{aligned}$$

Therefore

$$\lim_{\alpha\to 0} \frac{d\sigma_{K-N}}{d\Omega} = Zr_0^2 \left(\frac{1+\cos^2\theta}{2}\right) \tag{A.2}$$

The polar plot of the solution is peanut shaped, indicating that for low energies, where $\alpha << 1$, the differential cross section is peanut shaped.

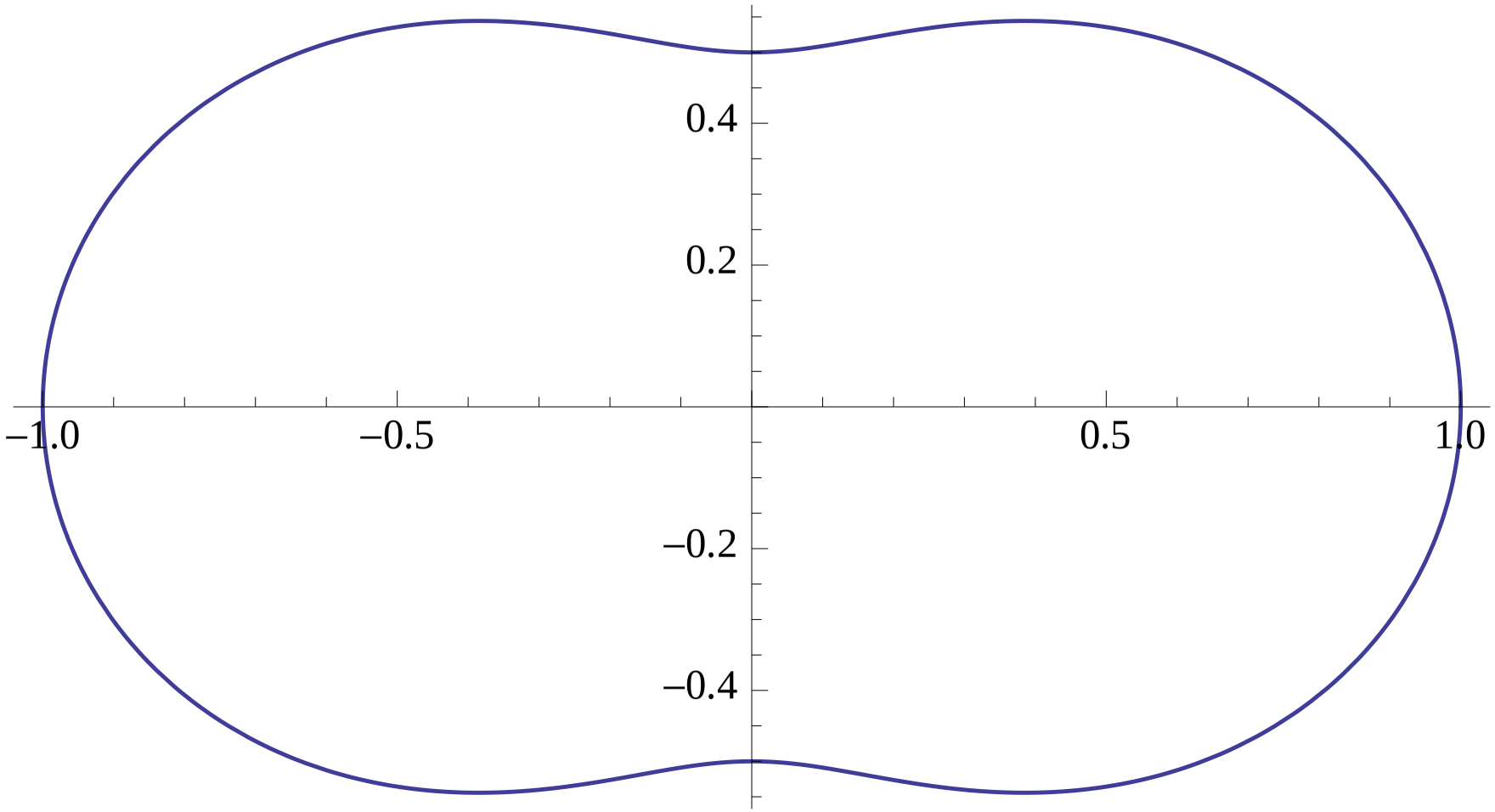

Figure A.1: The differential cross section shape in the limit of $E_\gamma = 0$

A.1.2 $\alpha \to \infty$

There are two cases

In the case where $1-\cos\theta \lessapprox {}^{1}/_{\alpha}$ there is the potential for critical points, if these points lead to a finite solution, then the condition is negligible. So consider the double limit

$$\lim_{\alpha\to\infty,\theta\to 0}\frac{d\sigma_{K-N}}{d\Omega} = Zr_0^2\cdot\lim_{\alpha\to\infty,\theta\to 0}\left(\frac{1}{1+\alpha(1-\cos\theta)}\right)^2\left(\frac{1+\cos^2\theta}{2}\right)\left(1+\frac{\alpha^2(1-\cos\theta)^2}{(1+\cos^2\theta)(1+\alpha(1-\cos\theta))}\right)$$

Consider

$$\lim_{\alpha\to\infty,\theta\to 0} 1+\alpha(1-\cos\theta) = 2$$

and

$$\lim_{\alpha\to\infty,\theta\to 0} 1+\cos^2\theta = 2$$

so

$$\lim_{\alpha\to\infty,\theta\to 0}\frac{d\sigma_{K-N}}{d\Omega} = Zr_0^2\left(\frac{1}{2}\right)^2\left(\frac{2}{2}\right)\left(1+\frac{1^2}{(2)(2)}\right) = \frac{5Zr_0^2}{16}$$

Which is finite.

In the general case where $1-\cos\theta > {}^{1}/_{\alpha}$ as $\alpha\to\infty$

$$\lim_{\alpha\to\infty}\frac{d\sigma_{K-N}}{d\Omega} = Zr_0^2\left(\frac{1+\cos^2\theta}{2}\right)\cdot\lim_{\alpha\to\infty}\left(\frac{1}{1+\alpha(1-\cos\theta)}\right)^2\left(1+\frac{\alpha^2(1-\cos\theta)^2}{(1+\cos^2\theta)(1+\alpha(1-\cos\theta))}\right)$$

We will consider

$$\lim_{\alpha\to\infty}\left(\frac{1}{1+\alpha(1-\cos\theta)}\right)^2\left(1+\frac{\alpha^2(1-\cos\theta)^2}{(1+\cos^2\theta)(1+\alpha(1-\cos\theta))}\right)$$

In the limit $\alpha >> 1$ this simplifies to

$$\lim_{\alpha\to\infty}\left(\frac{1}{\cancel{1}+\alpha(1-\cos\theta)}\right)^2\left(1+\frac{\alpha^2(1-\cos\theta)^2}{(1+\cos^2\theta)\left(\cancel{1}+\alpha(1-\cos\theta)\right)}\right)$$

which simplifies to

$$\lim_{\alpha\to\infty}\left(\frac{1}{\alpha(1-\cos\theta)}\right)^2\left(1+\frac{\cancel{\alpha^2}(1-\cos\theta)^{\cancel{2}}}{(1+\cos^2\theta)\left(\cancel{\alpha(1-\cos\theta)}\right)}\right)$$

and since $\alpha \gg 1$

$$\lim_{\alpha\to\infty}\left(\frac{1}{\alpha(1-\cos\theta)}\right)^2\left(1+\frac{\cancel{\alpha^2}(1-\cos\theta)^{\cancel{2}}}{(1+\cos^2\theta)\left(\cancel{\alpha(1-\cos\theta)}\right)}\right) = \frac{1}{\alpha(1-\cos\theta)(1+\cos^2\theta)}$$

Therefore

$$\begin{aligned}\lim_{\alpha\to\infty}\frac{d\sigma_{K-N}}{d\Omega} =& Zr_0^2\left(\frac{1+\cos^2\theta}{2}\right)\frac{1}{\alpha(1-\cos\theta)(1+\cos^2\theta)}\\ =& \frac{Zr_0^2}{2\alpha(1-\cos\theta)}\end{aligned}$$

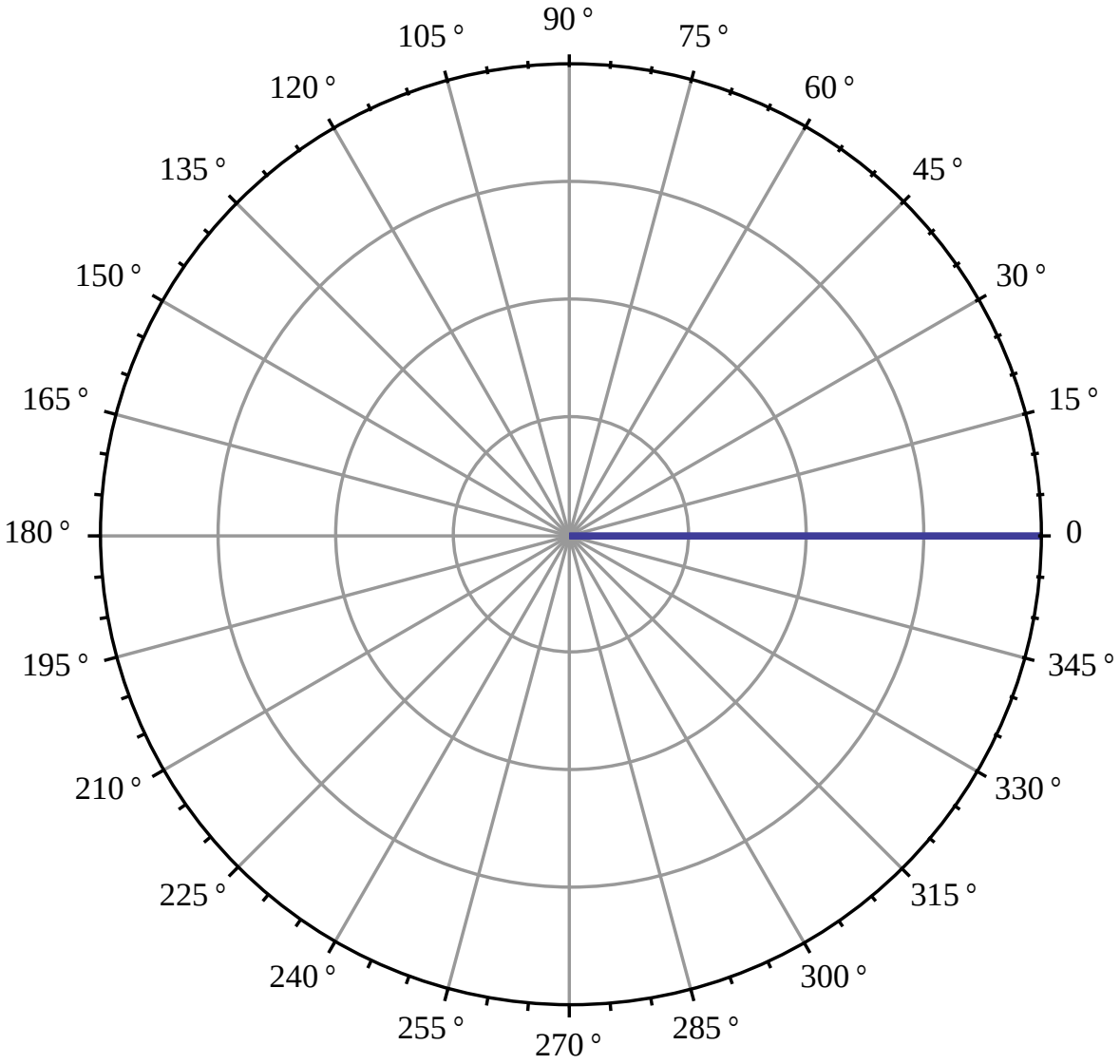

Figure A.2: The differential cross section shape in the limit of $E_\gamma = \infty$, shown as the blue line centred about the 0° of the polar plot

APPENDIX B

CODE

B.1 Mathematica workbook to calculate σ_{KN}

```
α[Egamma_]:=Egamma/m;

m = 0.510998928;

r = 2.8179403267 * 10^ - 15;

one[θ_, Egamma_] = 1/(1 + α[Egamma](1 - Cos[θ]))^2;

two[θ_, Egamma_] = (1 + (Cos[θ])^2)/2;

three[θ_, Egamma_] = 1 + α[Egamma]^2(1-Cos[θ])^2 / ((1+(Cos[θ])^2)(1+α[Egamma](1-Cos[θ])));

dσ[θ_, Egamma_, Z_]:=Zr^2 * one[θ, Egamma] * two[θ, Egamma] * three[θ, Egamma];

dσ[θ_, Egamma_]:=one[θ, Egamma] * two[θ, Egamma] * three[θ, Egamma];

dσN[θ_, Egamma_]:=dσ[θ, Egamma]/dσ[0, Egamma];
```

For Z = 1, the low energy limit of the fit approaches 0.665246 barns, which agrees with the Compton scattering low energy cross section limit ($E_\gamma \ll m_e$) known as the Thompson scattering cross section for a single electron.

```
LogLogPlot[10^28 * 2 * π * Integrate[dσ[θ, Eγ, 1] * Sin[θ], {θ, 0, π}], {Eγ, 0.005, 2},
{Frame → True, FrameLabel → {"Energy [MeV]", "σ [barns/atom]"}, ImageSize → Full,
AspectRatio → .5, LabelStyle → {FontFamily → "Helvetica"}}]
```

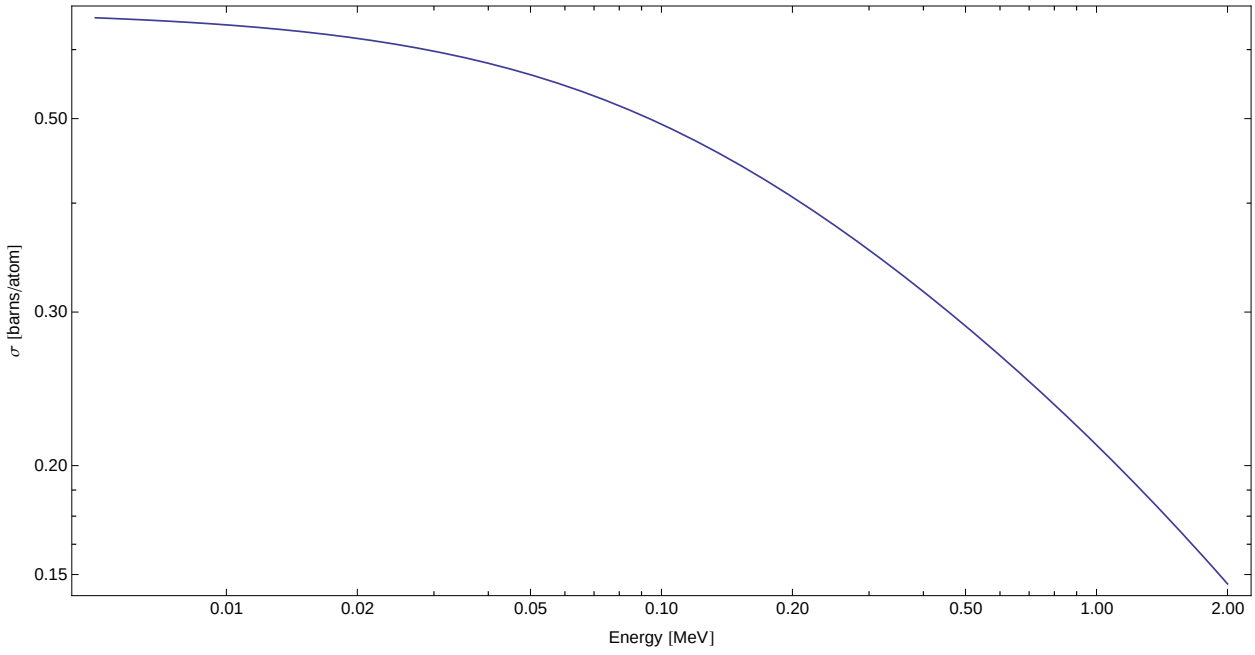

For Z = 6

```
LogLogPlot[10^28 * 2 * π * Integrate[dσ[θ, Eγ, 6] * Sin[θ], {θ, 0, π}], {Eγ, 0.005, 2},
{Frame → True, FrameLabel → {"Energy [MeV]", "σ [barns/atom]"}, ImageSize → Full,
AspectRatio → .5, LabelStyle → {FontFamily → "Helvetica"}}]
```

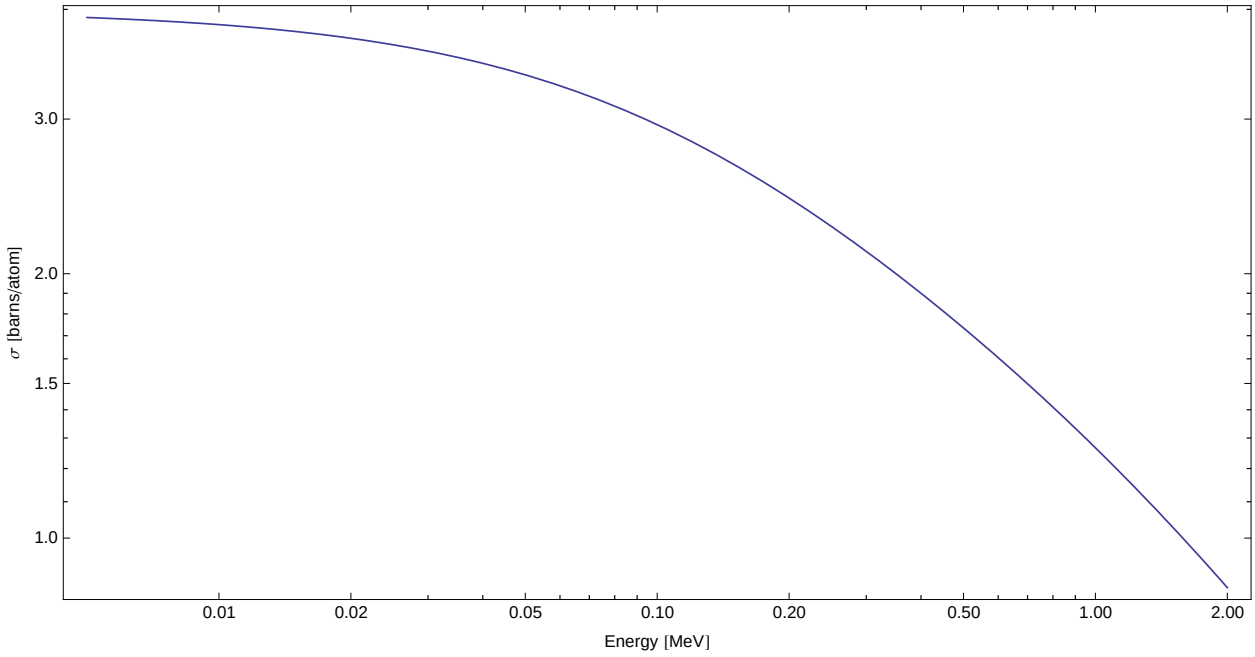

B.2 Finding a fit for XCOM using mathematica

To determine if a small enough window could be fit by a linear function, a the mass attenuation coefficient for a range of 0.2 keV around 59.5 keV was plotted and fit with the equation $y = ax + c$. The residual plot, seen at the end of Subsection B.2.1 shows a trend which indicates that linear is sufficient for interpolative purposes for a window of about 5 times the smallest significant figure XCOM will accept for energy resolution (XCOM is limited to four significant figures in energy).

B.2.1 Degree 1

```
data = {{0.0585, 1.704}, {0.0586, 1.696}, {0.0587, 1.689}, {0.0588, 1.681},
{0.0589, 1.673}, {0.059, 1.666}, {0.0591, 1.658}, {0.0592, 1.651},
{0.0593, 1.643}, {0.0594, 1.636}, {0.0595, 1.629}, {0.0596, 1.621},
{0.0597, 1.614}, {0.0598, 1.607}, {0.0599, 1.6}, {0.06, 1.593},
{0.0601, 1.586}, {0.0602, 1.579}, {0.0603, 1.572}, {0.0604, 1.565},
{0.0605, 1.558}};
nlm = NonlinearModelFit[data, (ax^2 + bx + c), {a, b, c}, x];
Show[ListPlot[data], Plot[nlm[x], {x, 0.0585, 0.0605}]]
nlm["ParameterTable"]
```

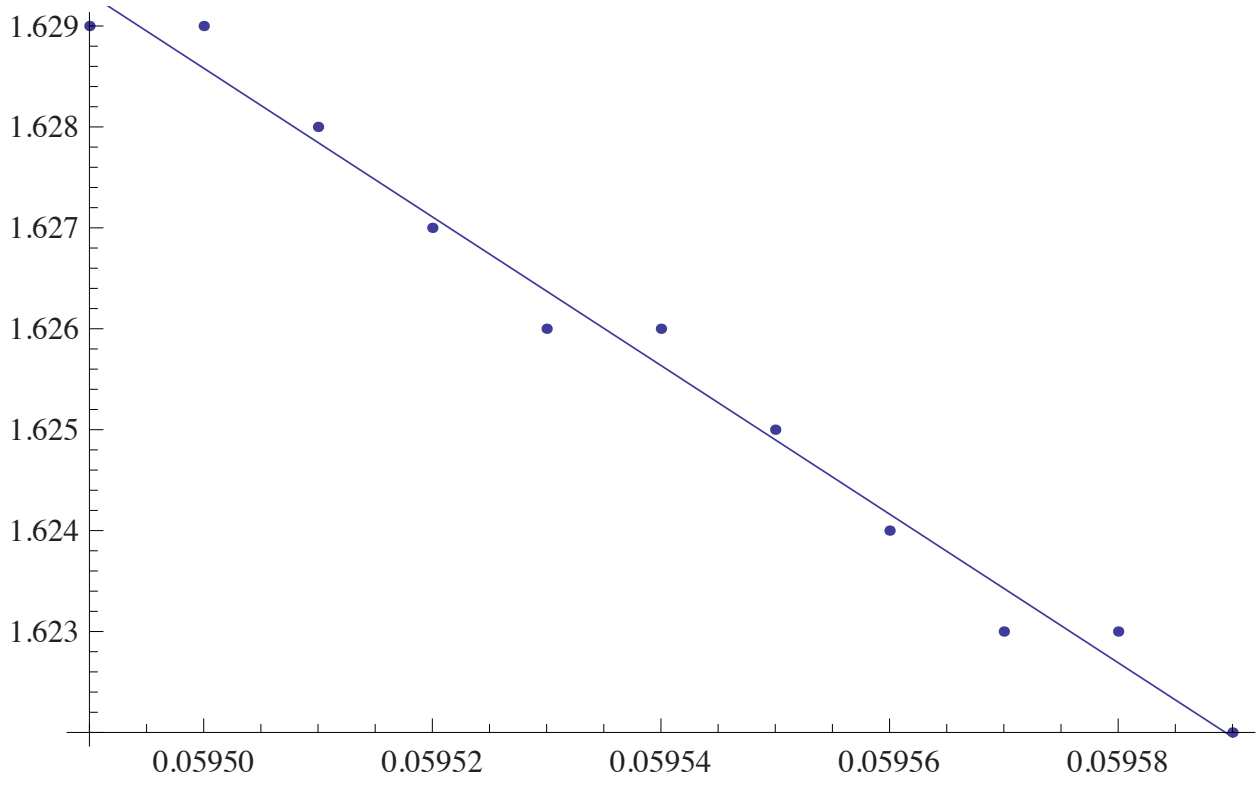

	Estimate	Standard Error	t-Statistic	P-Value
a	2447.32	166.837	14.6689	1.8715397304417726*^-11
b	−364.128	19.8539	−18.3404	4.2734258286101477*^-13
c	14.6301	0.590609	24.7713	2.329693640881663*^-15

nlm["FitResiduals"];

ListPlot[%, Filling → Axis]

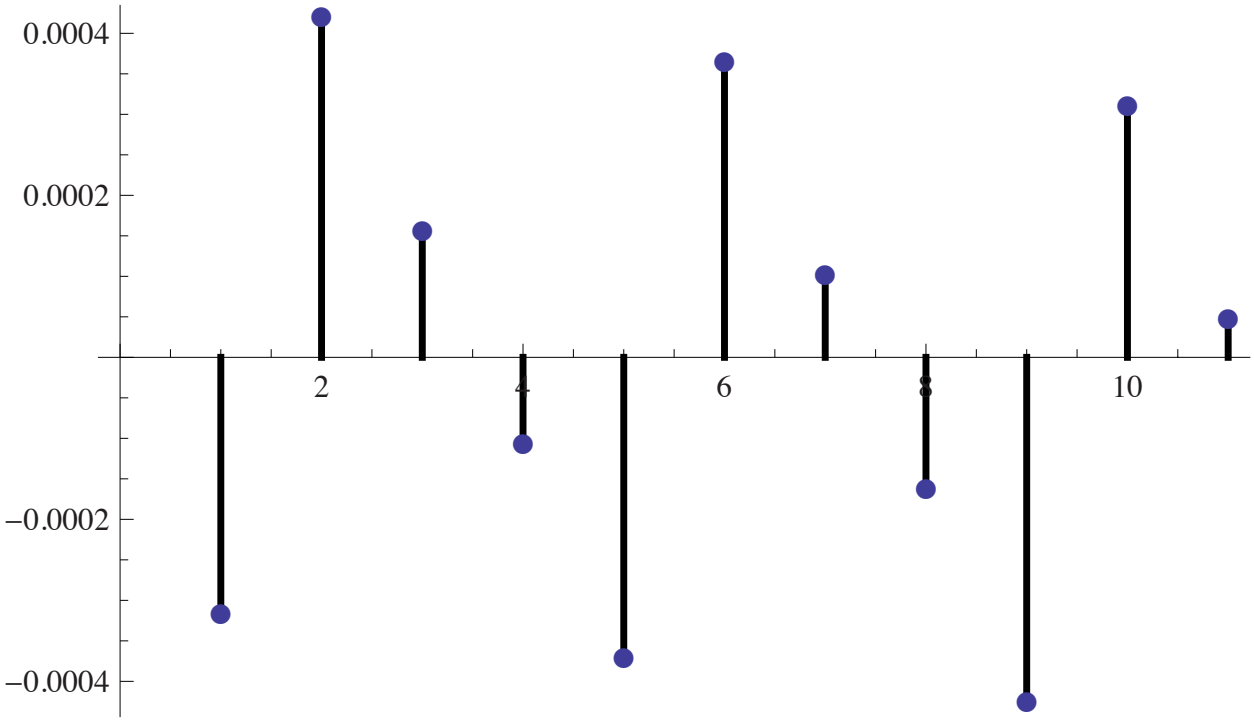

The final plot above, a residual plot, shows that there is no trend in the deviation of fit from the attempt to fit XCOM linearly for the range of 58.5 keV to 60.5 keV. This indicates that this range is small enough as to not be complicated with the larger trends of cross sections, and large enough to be used to calculate the inherent uncertainty in XCOM. The residual shows what could be a repeating pattern, indicative of rounding errors which could be tested by the coordinators of XCOM adjusting their intrinsic precision by one more significant figure in their calculation system.